Journal of Power Sources 196 (2011) 3204–3222

Contents lists available at ScienceDirect

Journal of Power Sources

journal homepage: www.elsevier.com/locate/jpowsour

A quasi-two-dimensional electrochemistry modeling tool for planar solid oxide fuel cell stacks

Kevin Lai[a,*], Brian J. Koeppel[a], Kyoo Sil Choi[a], Kurtis P. Recknagle[a], Xin Sun[a], Lawrence A. Chick[a], Vladimir Korolev[b], Moe Khaleel[a]

[a] Pacific Northwest National Laboratory, P.O. Box 999, Richland, WA 99352, USA
[b] Columbia Energy & Environmental Services Inc., Richland, WA 99352, USA

ARTICLE INFO

Article history:
Received 14 October 2010
Received in revised form 9 November 2010
Accepted 22 November 2010
Available online 26 November 2010

Keywords:
Solid oxide fuel cells (SOFCs)
Finite volume method
Numerical simulations
Mathematical modeling
Electrochemical reactions
Thermal analysis

ABSTRACT

A quasi-two-dimensional numerical model is presented for the efficient computation of the steady-state current density, species concentration, and temperature distributions in planar solid oxide fuel cell stacks. The model reduction techniques, engineering approximations, and numerical procedures used to simulate the stack physics while maintaining adequate computational speed are discussed. The results of the model for benchmark cases with and without on-cell methane reformation are presented with comparisons to results from other research described in the literature. Simulations results for a multi-cell stack have also been demonstrated to show capability of the model on simulating cell to cell variation. The capabilities, performance, and scalability of the model for the study of large multi-cell stacks are then demonstrated.

1. Introduction

A fuel cell is an electrochemical conversion device that produces electricity directly from oxidation of a fuel. Fuel cells are characterized by their electrolyte material and, as the name implies, the solid oxide fuel cell (SOFC) has an oxide ceramic electrolyte [1]. Some advantages of this class of fuel cell include high efficiency, electrolyte stability, fuel flexibility, low emissions, high power density, simpler fabrication compared to other cell types, and the availability of byproduct heat for cogeneration; however, the greatest disadvantage is the high operating temperature that results in mechanical/chemical compatibility issues, thermal stresses, and longer start-up and shut-down times. Fuel cell technology, including ceramic electrolytes, has existed for well over a century, and industrial research into fuel cell-based power sources has been ongoing since the late 1950s [2].

Over the last 30 years, research teams around the world have shifted more focus to solid oxide fuel cell technologies as evidenced by the rapid rise of research publications of which the bulk is related to SOFCs [3]. In the United States, the Solid State Energy Conversion Alliance (SECA) was formed by the U.S. Department of Energy in 2000, and partnerships were forged among industry, national laboratories, and academia to make SOFCs a cost-effective alternative power source [4–6]. As part of this expanding research effort, the physical phenomena occurring in SOFCs have been studied using numerical modeling to gain scientific understanding and engineering guidance. Numerical models are crucial to accelerating knowledge and understanding within any SOFC development activity because they complement the expensive and time consuming, but necessary, experimental testing. Fast and efficient numerical modeling can be used to perform virtual experiments that are important to cell design and stack operation, thereby reducing the resources and development time needed for a new SOFC concept.

Models for studying SOFCs at different length scales continue to be important to advance knowledge and understanding of how to improve performance, stability, reliability, and efficiency. Molecular and microstructural scale models have been important for understanding the fundamental electrochemical behaviors occurring in the cell and the effect of materials and structure on the cell performance (e.g., [7–11]). Cell and stack level models are essential for the SOFC designer to achieve good power output while minimizing temperatures and thermal gradients that lead to structural degradation or failure. Numerous cell/stack level models have been generated to evaluate the coupled flow, electrochemical, and thermal behaviors of various stack geometries (e.g., [12–15,17–19]). SOFCs are desirable for power generation [16], so system-level models are used to obtain the operating conditions and controls necessary to achieve the highest possible efficiency for the SOFC or

* Corresponding author. Tel.: +1 509 372 6461; fax: +1 509 372 6099.
E-mail address: kevin.lai@pnl.gov (K. Lai).

0378-7753/$ – see front matter © 2010 Elsevier B.V. All rights reserved.
doi:10.1016/j.jpowsour.2010.11.123

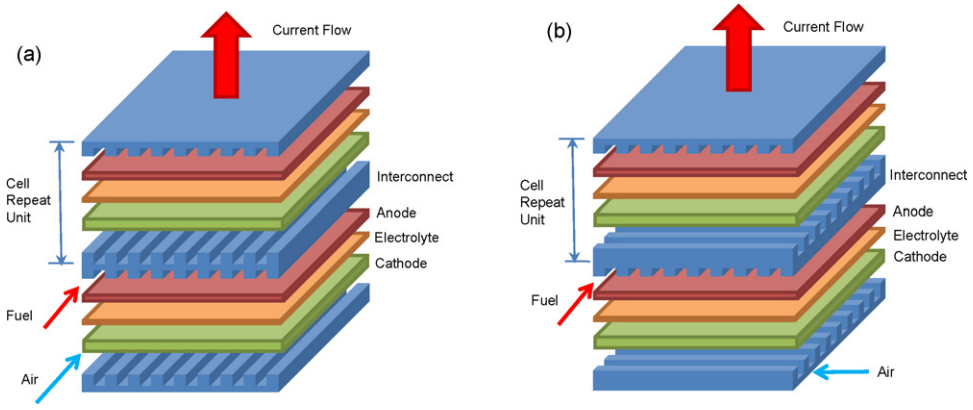

Fig. 1. Illustration of (a) co-flow/counter-flow and (b) cross-flow planar SOFC.

hybrid generation systems based on the unique operating requirements of the SOFC module [20]. More extensive reviews of the fundamental mathematical models for fuel cells and developed SOFC numerical models have been compiled by various authors [16,21–25].

The work presented in this paper attempts to bridge the stack and system levels by bringing internal spatial resolution to a computationally feasible submodel for use in system level studies. Other researchers have also recognized the need to move away from the typical zero-dimensional (0D or 1D, 2D, or 3D for one-, two-, or three-dimensional) thermodynamic models that provide performance based solely on the stack average state to create efficient numerical models that resolve internal distributions [26–28]. In prior work by the authors, tools that solve the coupled electrochemistry, thermal, and flow analysis for realistic 3D cell geometries were created in both the computational fluid dynamics (CFDs) and finite-element frameworks [13,29]. While tubular [30,31], microtubular [32–35], flattened tubular [36], and segmented-in-series cells [37] are being pursued by multiple teams and remain active viable concepts for SOFC geometries, the authors have focused primarily on planar designs, which exhibit the highest power density.

While the 3D model is extremely useful for engineering design of the cell geometry or short-stack performance, the computational requirements for detailed modeling of modern tall stacks increases dramatically. Stack developers using SOFCs for megawatt-scale power generation applications are striving for larger and taller stacks to reduce costs where 30-kW modules of nearly 200 cells in series are being operated, and planar areas approaching 1000 cm^2 are being evaluated [38,39]. To achieve the high efficiencies for SOFC or hybrid SOFC-turbine power plants using system modeling, models beyond purely thermodynamic calculations are needed to identify peak internal temperatures or current densities important to stack reliability. Toward this end, the 3D numerical model developed previously can be reasonably simplified to a more computationally efficient 2D model for symmetric flow configurations. In this paper, we present such a model that more rapidly computes the solution for symmetric multi-cell stacks while still providing spatial resolution for the temperature, current, and species distributions along the direction of gas flow.

2. Model descriptions and assumptions

Simulating the SOFC stack operation requires consideration of multiple physical phenomena, such as heat transfer, mass transfer, charge transfer, chemical reactions, electrochemical behavior, and structural deformation. Since fully coupled computational models considering all of the above fields simultaneously with high fidelity are not yet available, existing SOFC modeling efforts have been focusing on specific aspects of the SOFC operation or design with available computational resources. For example, prior work within the authors' modeling group developed simulation tools to evaluate the electrochemical performance of 3D cell geometries [13,29], and the predicted thermal fields were subsequently used for mechanical stress analyses to assess structural performance [39–41].

While the detailed 3D model will provide information from the stack-level fuel/oxidant outlet temperatures or power output as a function of stack temperature, its computational cost is usually high for solving large multi-cell stack towers for megawatt-scale power generation systems, for which case a faster modeling tool would be more desirable. On the other hand, existing system-level models typically offer no spatial resolution, resulting in a 0D or 1D result that neglects important thermal gradients and mischaracterizes the temperature state of the stack.

The objective of this effort was therefore to provide an efficient computational tool that can provide the users with distributions of the current density, voltage, species concentration, and temperature within the multi-cell stack. The ability of the user to define all model parameters, material properties, boundary conditions, and current–voltage relationship is still required as well as the capability to study the effect of multiple cells stacked in series. The developed tool has proven to be useful in characterizing the thermal state of SOFC stacks of up to 100 cells with computation durations measured in minutes rather than hours or days. This paper discusses a quasi-2D SOFC multi-physics model (SOFC-MP) that solves the coupled electrochemistry analysis and heat transfer calculations in a 2D cross-section of the stack to give detailed internal profiles of temperature, current density, flow compositions, and cell voltage distribution. This is based on the user-defined geometry, initial flow conditions, SOFC electrochemistry, and boundary conditions. The basis, assumptions, formulation, and numerical implementation of this model and demonstrations of its capabilities are described in the following sections.

2.1. Assumptions for the quasi-two-dimensional approximation

Many SOFC manufacturers, including several of the SECA program participants, have used the planar configuration [6], so this has been the primary geometry of interest for the authors. In the traditional planar design, the fuel and air channels can be arranged in co-flow, counter-flow, or cross-flow configurations to supply the fuel and oxidant in the most efficient manner to maximize power and minimize temperature gradients within the stack (Fig. 1). A 3D model is required for detailed evaluations or subsequent structural analyses, but it is nevertheless computationally expensive. However, when only co-flow or counter-flow cases are considered, the

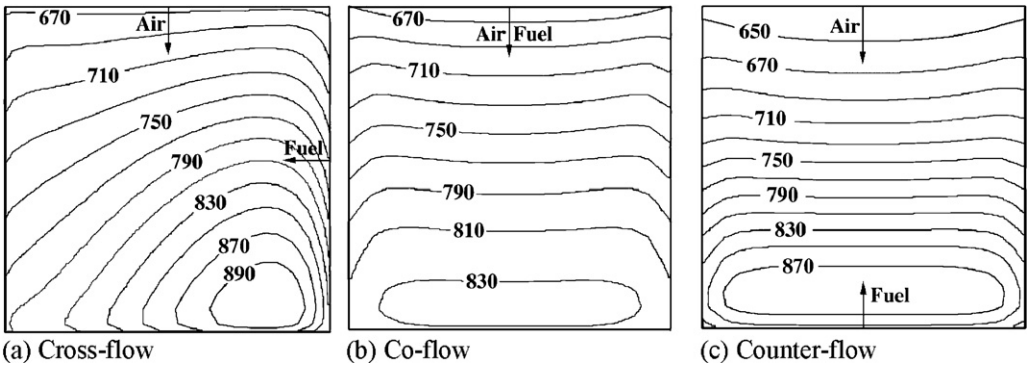

Fig. 2. Temperature distribution (°C) in the active cell for (a) cross-flow, (b) co-flow, and (c) counter-flow configurations [6].

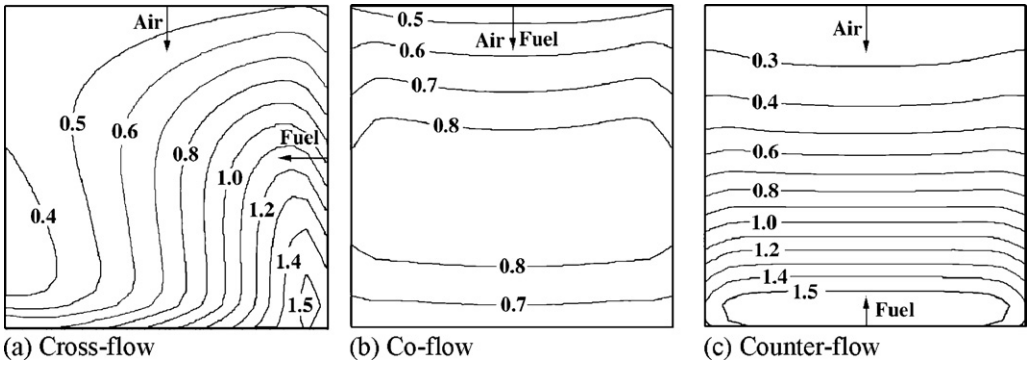

Fig. 3. Current density distribution (A cm^{-2}) in the active cell for (a) cross-flow, (b) co-flow, and (c) counter-flow configurations [6].

3D model can often be reasonably approximated by a 1D or 2D model for engineering purposes with the following assumptions on the flow, thermal, and electrochemical behaviors.

The first assumption is that the physical fields across the width direction, perpendicular to the flow direction, remain largely unchanged. For example, detailed 3D results of Recknagle et al. [29] presented contour plots for temperature, species concentration, and current density distributions over the cell surface with the fuel and air in co-flow, counter-flow, and cross-flow configurations. All of the computational results, including the temperature, hydrogen concentration, and current density fields shown in Figs. 2–4, are quite uniform across the width direction for the co-flow and counter-flow cases. Similar observations can be made from other modeling results [12,28,42–43]. Since these primary results of interest show little variations in the width direction, the actual 3D problem can be reasonably approximated by a 2D solution. The assumption becomes less appropriate as the heat loss to the sides becomes more significant or as the cell area becomes very small. Nevertheless the assumption should be generally valid for large, well insulated cells that are nearly adiabatic.

The second assumption is that the thickness dimensions of a cell are small, and the physical properties in the thickness direction are constant for each domain in the cell (fuel channel, air channel, interconnect, and the positive electrode/electrolyte/negative electrode (PEN) assembly). For the solid PEN and interconnect structures, temperature variation through the thickness is assumed to be small. For fuel and air gas channels, the mass transport is treated as a fully developed laminar flow described sufficiently by its mean velocity and temperature. Therefore, through-thickness gradients in these domains are ignored, but temperature differences between these domains are permitted based on the thermal transport mechanisms. This assumption leads to further simplification of our model such that only four control volumes are used along the out-of-plane direction of the cell, e.g., interconnect, fuel, PEN, and air. Since the interconnect serves a dual purpose as the gas barrier and the current collector, it often has a complex struc-

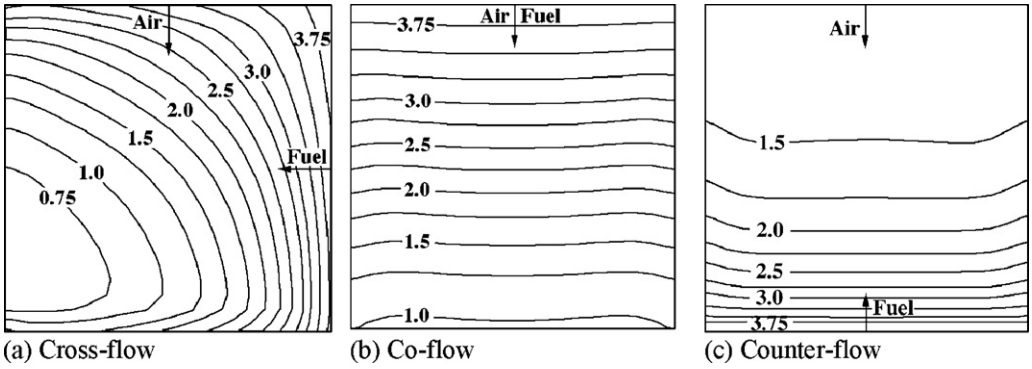

Fig. 4. Hydrogen mass distribution (%) in the active cell for (a) cross-flow, (b) co-flow, and (c) counter-flow configurations [6].

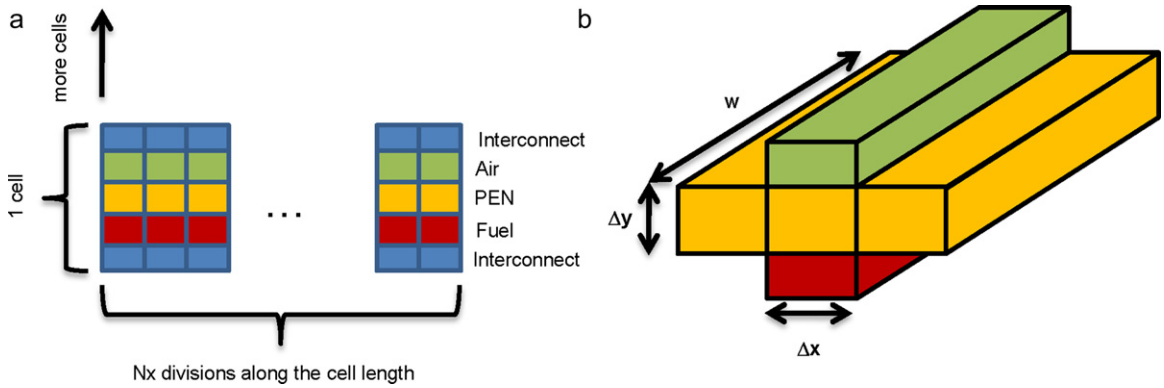

Fig. 5. Illustration of SOFC-MP 2D mesh.

ture (e.g., ribs, channels, mesh, stamping) that permits flow while transmitting current between a series of connected cells. In SOFC-MP 2D, effective properties are used instead of explicitly modeling the geometric details of interconnect to include their influence on conductive heat transfer and electrical conductivity. These simplifications enable a drastic improvement in computational efficiency while sufficiently capturing the on-cell spatial distribution of temperature and the contribution to ohmic loss between cells.

With these assumptions, we derive a model where property values along a 1D path along the flow direction are calculated for four domains in each cell: the fuel stream, the air stream, the anode–electrolyte–cathode structure, and the interconnect. The quasi-2D model is then assembled by stacking multiple 1D paths through the thickness direction to simulate a multi-cell SOFC stack. The associated computational grid for the cell is schematically depicted in Fig. 5(a). This arrangement is best characterized as a quasi-2D solution, but the model will subsequently be referred to here as SOFC-MP 2D (to differentiate it from the existing 3D model).

In the electrochemistry model, the PEN layers are represented with one computational point where a current–voltage relationship is implemented. Due to the low ionic conductivity of the electrolyte relative to the high electrical conductivity of the anode and interconnect, the ohmic voltage drop in the electrolyte is much greater than the ohmic drop in the anode and interconnect. This permits the code to assume that an entire planar PEN is at the same working voltage. The working voltage for each cell in the stack can then be calculated without the need for a full electric field computation. The current–voltage relationship at each computational point is then used to obtain the cell's current density distribution based on the local species concentrations, temperature, and cell voltage.

Finally, we assume that the stack operates at steady state with the initial configuration and virgin material properties. In other words, the model will solve the electrochemistry problem without considering any structural changes or material degradations caused by the high operating temperature of the stack. The thermal deformations/stresses at the component level and degradation mechanism processes at the microstructural level in the fuel cell are other important areas pursued by SOFC researchers because the structural response obviously depends on the electrochemical performance. Usually though, structural deformations are assumed to be small enough such that the effect on gas flow and electrochemical performance is minimal.

3. Governing equations

The governing equations describing the electrochemistry, heat transfer, and fluid flow are given below along with a brief description of the underlying assumptions. More in-depth discussion on these topics can be found in the references on system models and stack/cell level models (e.g., [13,44]). Overall, the electrochemistry (EC) model provides the user with the power output, species utilizations, and temperature results that are necessary to make engineering decisions on the design and operation of multi-cell stacks.

3.1. Electrochemistry

The EC model in SOFC-MP simulates the cell electrochemical behavior through a current–voltage relationship, which provides the cell operating voltage as a function of current density, temperature, cell properties, and local species concentrations. The general form of the current–voltage relationship consists of the Nernst voltage (V_{Nernst}) minus the ohmic (η_{ohmic}), activation ($\eta_{\text{activation}}$), and concentration ($\eta_{\text{concentration}}$) polarizations:

$$V_{\text{cell}} = V_{\text{Nernst}} - \eta_{\text{ohmic}} - \eta_{\text{activation}} - \eta_{\text{concentration}} = f(i) \tag{1}$$

The Nernst voltage for a hydrogen fuel consists of the reversible open circuit voltage, computed from the change of Gibbs free energy for H_2 oxidation at standard pressure at the operating temperature, with adjustment for the actual system pressure and gas concentrations used. The Nernst potential assuming atmospheric fuel and oxidant pressures is given by

$$V_{\text{Nernst}} = \frac{\Delta G_f}{2F} + \frac{R_G T}{2F} \ln\left(\frac{p_{\text{H}_2} {p_{\text{O}_2}}^{1/2}}{p_{\text{H}_2\text{O}}}\right) \tag{2}$$

where ΔG_f is the enthalpy change of formation for the reaction at the local temperature, F is the Faraday constant, R_G is the gas constant, T is the temperature, and p_{H_2}, p_{O_2}, $p_{\text{H}_2\text{O}}$ are the hydrogen, oxygen, and water partial pressures, respectively. Two methods for inputting the current–voltage (I–V) relationship are implemented. First, the approach used previously in other modeling activities [29,45] is implemented as the default calculation method. This form shown in Eq. (3) calculates the cell operating voltage by computing terms corresponding to the local Nernst potential, ohmic resistance, activation polarization, cathode O_2 concentration polarization, anode H_2 concentration polarization, and anode H_2O concentration polarization as

$$V_{(i)} = V_{\text{Nernst}} - iR_i - b\sinh^{-1}\left(\frac{i}{2i_0}\right) + \frac{R_G T}{4F}\ln\left(1 - \frac{i}{i_{\text{O}_2}}\right) + \frac{R_G T}{2F}\ln\left(1 - \frac{i}{i_{\text{H}_2}}\right) - \frac{R_G T}{2F}\ln\left(1 + \frac{p^0_{\text{H}_2} i}{p^0_{\text{H}_2\text{O}} i_{\text{H}_2}}\right) \tag{3}$$

where V_{Nernst} is the Nernst potential, i is the current density, R_i is the Ohmic resistance, $b\sinh^{-1}(i/2_{i_0})$ is the activation polarization, R_G is the gas constant, T is the temperature, F is the Faraday constant, i_{O_2} is the oxygen transport limiting current, i_{H_2} is the hydrogen

transport limiting current, and $p^0_{H_2O}$ and $p^0_{H_2}$ are the water and hydrogen partial pressures, respectively. The activation polarization is described by a Butler–Volmer formulation where

$$b\frac{R_G T}{\alpha F} \tag{4}$$

where α is the transfer coefficient, and the exchange current density i_0 is given by

$$i_0 = P_x \exp\left(\frac{-E_a}{R_G T}\right) \tag{5}$$

where E_a is the activation energy and P_x is a pre-exponential constant. The limiting currents calculated here assume that the dominant mode of gas transport in the anode and the cathode is by bulk diffusion through uniform microstructures of characteristic porosity and tortuosity [13,44]. The limiting current for the specie i_x is given by

$$i_x \frac{2FD_x^{\text{eff}} p_x}{RTt_x} \tag{6}$$

where D_x^{eff} is the effective diffusion coefficient, p_x is the partial pressure, t_x is the electrode thickness, and subscript x denotes the corresponding species of H_2, O_2, or H_2O. Finally, the resistance of the stack structure is computed from the layer resistances as $R_i = R_p + R_e + R_n + R_b$, where R_p is the cathode electrical resistance, R_e is the electrolyte ionic resistance, R_n is the anode electrical resistance, and R_b is the bipolar plate electrical resistance.

Since Eq. (3) may not be suitable for all users who want to implement their own proprietary electrochemical routines or experimental data, the second option is a user-defined electrochemistry subroutine. The subroutine is written in an interpreted language Lua [49], which permits the subroutine to be compiled directly upon execution of SOFC-MP. This permits the user-subroutine to be of any mathematical functional or tabular form that returns only the appropriate voltage based on the local temperature, species partial pressures, and current density arguments sent from the main solver algorithm. Details of the Lua interface for user-defined inputs are discussed in Section 3.3.2.

The EC model in SOFC-MP is also capable of simulating electrochemical reactions with composite fuel mixtures containing H_2, H_2O, CO, CO_2, N_2, and/or CH_4. For mixed fuels, it is assumed in this model that the amount of CO or CH_4 that is electrochemically oxidized is small and only H_2 is oxidized [44]. Li and Chyu [46] showed that electrochemical oxidation of both CO and H_2 at the anode yields the same Nernst potential in the SOFC as long as the water-gas shift reaction is in equilibrium. This was confirmed experimentally by Weber et al. [47] who observed similar electrochemical performance with direct H_2, CO, and CH_4 oxidation as long as carbon deposition was suppressed. Matsuzaki and Yasuda [48] showed that experimental oxidation rates for H_2 were two to three times faster than CO for the Ni:YSZ anode/YSZ electrolyte system. Therefore, the model assumes that the CH_4 reformation rate is kinetically controlled, the water-gas shift reaction is fast and always in chemical equilibrium, and that fuel cell only oxidizes H_2. Since the mixed fuels of interest in this work are typically compositions with a significant molar fraction of H_2 and a steam-to-carbon ratio of 2–3 is used for any carbon species fuels, the same formulation for the I–V relationship in Eq. (2) can thereby be used.

3.2. Conservation of mass/species

The generic transport equation for conservation of species concentration c_i is given by

$$\frac{\partial \rho c_i}{\partial t} = \nabla \cdot (\rho \vec{V} c_i) = \nabla \cdot \vec{J} + S_i \tag{7}$$

with terms that provide, respectively, the change of concentration and density ρ with time t, advection due to the velocity field $\vec{V}$, diffusive flux due to concentration gradients $\vec{J}$, and species sinks/sources S_i The EC module simplifies the gas transport problem by assuming the gas channels are incompressible, steady-state, 1D, constant velocity flows where mass diffusion is small relative to the bulk advection, resulting in the following relation for species conservation:

$$\rho v \frac{\Delta c_i}{\Delta x_i} = S_i \tag{8}$$

where ρ is the density, v is the velocity along the flow direction, and S_i is the species sink/source due to the electrochemical reactions. This formulation circumvents the need to solve the complete fluid flow problem involving the Navier–Stokes equations and hence results in significantly improved computational efficiency.

When an appropriate I–V model is specified, the current density, i, can be calculated from the assumed cell voltage, fuel temperature, and gas species composition. The overall cell reaction for the oxidation of hydrogen is

$$H_2 + \frac{1}{2}O_2 \rightarrow H_2O \tag{9}$$

The corresponding oxygen and hydrogen consumption rates [50] for a stack with N cells are

$$\dot{n}_{O_2} = \frac{I}{4F} = \frac{iNA}{4F}\text{moles s}^{-1} \quad \dot{n}_{H_2} = \frac{I}{2F} = \frac{iNA}{2F}\text{moles s}^{-1} \tag{10}$$

where I is the current generated for the specific control volume and A is the active area. Each mole of oxygen oxidizes two moles of hydrogen to produce two moles of water and two electrons. The change to the local molar flow rates for the hydrogen, water, and oxygen species can then be easily obtained.

When CO is added to the fuel, the water-gas shift reaction converts CO into H_2 according to the following reaction:

$$CO + H_2O \rightarrow H_2 + CO_2 \tag{11}$$

The reaction is assumed to be fast, such that the species composition quickly reaches local equilibrium based on a temperature-dependent equilibrium constant computed from the free energy of the reaction:

$$K_{\text{shift,CO}} = \frac{P_{H_2}P_{CO_2}}{P_{H_2O}P_{CO}} = \exp\left(\frac{\Delta G_{\text{shift}}}{RT}\right) = \exp\left(-\frac{\sum_{\text{products}}(H_i - TS_i) - \sum_{\text{recatants}}(H_i - TS_i)}{RT}\right) \tag{12}$$

where the change in free energy ΔG_{shift} is computed using the changes in enthalpy H_i and entropy S_i for each of the participating species in the reaction. With both hydrogen and carbon monoxide in the fuel, the fuel composition along the flow direction is obtained by simultaneously solving the shift equilibrium and oxygen consumption rate equation for each control volume marching along the flow direction. Since the user may implement any arbitrary fuel composition into the model, highly non-equilibrated fuels containing CO would shift rapidly at the fuel inlet region with high heat outputs. The model also includes a user-defined distance parameter over which the fuel composition is allowed to progress from the initial state to full equilibrium where the local value of $K_{\text{shift,CO}}$ changes linearly from the value at the inlet to the equilibrium value. Generally, testing with various realistic fuel compositions showed few numerical issues due to other solution control mechanisms that aid stable convergence. If methane is added to the fuel, steam reformation occurs, which is an endothermic reaction where CH_4

is catalyzed by the nickel in the anode cermet:

$$CH_4 + H_2O \rightarrow 3H_2 + CO \quad (13)$$

The reformation reaction is kinetically controlled. Rate equations are difficult to obtain experimentally, but various relationships for Ni:YSZ anodes have been established from experiments for use in modeling efforts. Xu and Froment [51], Achenbach and Riensche [52,42], Dicks et al. [53], and Ahmed and Foger [54] calculated the reaction rate of methane according to an empirical formula derived from experiments. At cell operating temperatures, the methane reforming occurs relatively quickly until the composition reaches equilibrium. The Achenbach and Riensche relation [52] is implemented as the default reforming rate equation, but any user relation can be implemented through a Lua subroutine. The equilibrium constant is defined similarly to that for the water-gas shift reaction as

$$K_{\text{shift},CH_4} = \frac{p_{H_2}^3 p_{CO}}{p_{CH_4} p_{H_2O}} \quad (14)$$

and the value of K_{shift,CH_4} is calculated from the change in free energy for the reaction components in the same way as described above for CO.

SOFC-MP provides three approaches for the simulation of methane reforming. Because methane reforming is an endothermic reaction, the temperature field and simulation result near the fuel inlet area are sensitive to the reforming model chosen. The first approach applies a default reforming rate as described above, e.g., one provided by Achenbach [42]. The methane reforms along the flow path according to the computed reaction rate until equilibrium is reached, and the gas compositions remain fully equilibrated for the rest of the fuel flow. In addition to the default reforming rate, the model also allows users to define their own reforming rate expression through a Lua interface, which will be discussed in Section 3.3.2. Another approach is to assume that the methane reforming reaction is also relatively fast and can be approximated with the equilibrium-path-length approximation described above for CO. For example, the fuel composition described in Section 5.1.2 that initially contains 17% methane has an equilibrium value of less than 0.01% methane at high operating temperatures above 900 °C. The numerical result from the reforming rate approach using the Achenbach rate expression indicates that the composition of CH_4 is 90% consumed at about 5–10% of the 10 cm cell length, although full equilibrium is not reached until 20% of cell length. These results indicate that the equilibrium path approach with a reasonable percentage cell length based on available experimental observations could be a good alternative when a rate expression is difficult to obtain. By balancing the fuel species to equilibrium according to the current density calculated by the *I–V* relationship, the coupling between the fluid flow and the electrochemical reactions is thus achieved, and it is used to satisfy the mass and species balance for each computational point.

3.3. Conservation of energy

The temperature distribution of an SOFC has a very important effect on its performance (e.g., [50,55]) since the thermal-physical properties, electrochemistry performance, and gas species equilibrium composition is all tightly coupled with the temperature. Solving the thermal energy balance is thus one of the major tasks in the SOFC-MP model. Heat is primarily generated from the electrochemistry reactions where oxidation of H_2 and the CO water-gas shift are exothermic reactions while CH_4 steam reformation is endothermic. Joule heating is also created in the solids because of ohmic resistance. To prevent excessive temperatures in the stack, this generated heat must be dissipated through convective cooling provided by the fuel and oxidant flows and/or exterior losses to the environment. Typically in most designs, oxidant flow rates are increased to provide sufficient cooling through forced convection. The heat transfer mechanisms included in the model are (1) conduction in the cell and interconnect, (2) convection between the cell/interconnect and the fuel/oxidant flows, (3) advection within the fuel/oxidant flows, (4) radiation between the cell and interconnect, (5) radiation/convection between the cell and insulated enclosure, and 6) radiation/convection from the insulated enclosure to the external environment.

SOFC-MP contains a core algorithm that solves the steady-state heat transfer problem by the finite-volume method to provide the temperature distribution in the entire fuel cell stack. Considering the entire model domain, the enthalpy changes within the stack, the electrical power output, and the heat loss to the environment are balanced until the steady-state solution is achieved. The EC model is coupled to the heat transfer model through the assigned current–voltage relationship that defines the usable electrical power based on the voltage of each volume representing the cell. The enthalpy of the gases is computed using the standard Chemical Equilibrium with Applications (CEAs) FORTRAN property library [56,57]. For the assigned *I–V* performance, all the volumetric heat generated (or absorbed) from the H_2 oxidation, CO shift, and CH_4 reforming reactions as well as the Joule heating and polarization losses are accounted for in the enthalpy change calculation.

The heating rate due to the enthalpy change with time, $(\Delta H/\Delta t)$, from advection of species through a computational volume or the ionic transport of the O_2 is then

$$\frac{\Delta H}{\Delta t} = \sum \dot{n}_j M_j h_j \quad (15)$$

where $\dot{n}_j$ is a molar flow rate, M_j is the molar mass, h_j is the specific enthalpy, and j is summed over the number of present species. The heat transfer rates between adjacent volume elements are computed with conventional equations for solid conduction Eq. (16), solid-gas convection Eq. (17), solid-solid gap radiation Eq. (18), and radiation to the ambient Eq. (19):

$$q_{\text{conduction}} = -kA\frac{T - T_n}{\Delta x} \quad (16)$$

$$q_{\text{convection}} = -h_c A(T - T_n) \quad (17)$$

$$q_{\text{gap\_radiation}} = -4\varepsilon_1\varepsilon_2\sigma A T^3(T - T_n) \quad (18)$$

$$q_{\text{ambient\_radiation}} = -4\varepsilon\sigma A T^3(T - T_a) \quad (19)$$

where k is thermal conductivity, h_c is the convective film coefficient, T is the local temperature, T_n is the temperature of the neighboring volume element, T_a is the ambient environment temperature, A is the area of the element face through which the heat flux is calculated, Δx is the conduction length, ε is emissivity, and σ is the Stefan–Boltzmann constant. The usable electrical power P_{elec} is simply

$$P_{\text{elec}} = ViA_{\text{cell}} \quad (20)$$

where V is the cell operating voltage, i is the cell average current density, and A_{cell} is the cell active area. Therefore, the energy balance for the generic finite volume is thereby established by

$$\frac{\Delta H}{\Delta t} + \sum(q_{\text{condition}} + q_{\text{convection}} + q_{\text{gap\_radition}} + q_{\text{ambient\_radition}}) + P_{\text{elec}} = 0 \quad (21)$$

where only the terms corresponding to the appropriate thermal transport mechanisms (Eq. (15) through Eq. (20)) active in each volume of interest are used, and energy is locally conserved in every volume element. The electrochemical reactions are assumed

to occur within the anode, so the heat from the enthalpy change is assigned to the PEN structure.

During the solution process, the maximum temperature difference between iterations for every point is checked until it is reduced below a user-defined convergence tolerance. The global energy balance for the entire stack can then be validated after the solution by comparing the net chemical energy $Q_{reaction}$, useful electrical power P_{elec}, enthalpy changes of the outlet fuel/oxidant streams Q_{gases}, and exterior heat losses Q_{loss} according to the following relation:

$$\Delta E_{imbalance} = \frac{\Delta H}{\Delta t} + P_{elec} + Q_{loss} = Q_{reaction} + Q_{gases} + P_{elec} + Q_{loss} \approx 0 \quad (22)$$

3.3.1. Boundary conditions

The model computes the stack temperature distribution based on the input properties of the fuel and air streams, the operating voltage, and the heat loss to its surroundings. The inlet composition, inlet temperature, and flow rates of the fuel and air streams are defined by the user.

The model has the capability to define external thermal boundary conditions that mimic the cell placement within a furnace or an insulated enclosure. These boundary conditions account for heat transfer by convection and radiation from the stack to its surroundings. For the furnace condition, the convective heat transfer coefficient, ambient air temperature, stack emissivity, and furnace temperature are defined for the exterior of the stack. Values may be assigned independently for the bottom, top, front, back, and sides of the stack. If the stack is contained within an insulated enclosure, additional values for the insulation thermal conductivity, thickness, convection coefficient between the stack and insulation, and emissivity of the insulation are also defined for each side in addition to the previous external boundary conditions. Furthermore, variation of the inlet temperature of air and fuel from the bottom to the top of the stack can be specified to best mimic the actual operating environment if desired.

3.3.2. User-defined inputs

Different cell designers will likely have different modeling approaches for simulating the *I–V* curve for their cells. For flexibility, a well designed ability to work with a broad spectrum of user-defined electrochemistry models is desirable. Therefore, a general SOFC modeling program must not be constrained by using only one specific model and equation set. The capability to include customized electrochemistry models is implemented in the SOFC-MP model. This flexibility also works well on the principle that SOFC-MP users do not desire to share their proprietary information with software developers and other users. For this purpose, programming language Lua [49] was chosen as the designated language for user electrochemistry subroutines that interface with SOFC-MP. The choice of Lua was made because of its relatively simple C application program interface (API), popularity, ease of use, and availability of support. For SOFC-MP, the primary Lua interface is for a user model to calculate voltage based on the current density, temperature, and species composition parameters, but other interfaces have been developed as needed to implement customized thermal-physical properties or control the methane reformation rate.

4. Numerical algorithms and implementation

The 2D EC module for the fuel cell was programmed in Visual Studio C++ 2008 for Windows and GNU C++ for Linux, interfacing with many subroutines written in FORTRAN 77. The program is currently in standalone format, but it can be readily converted into a library or a dynamic-link library (DLL) to be integrated with a more comprehensive SOFC system-level model.

The multi-cell stack SOFC is modeled in 2D control volumes as shown in Fig. 5. Assuming the number of cells is N_{cells}, and the numerical increment in the flow direction is N_x, there will be a total of $(4N_{cells} + 1)N_x$ control volumes for the whole SOFC stack in our finite volume method (FVM) solution scheme.

The solution starts with an initial guess on the temperature field and cell voltage based on inlet air and fuel temperature as well as the average cell voltage specified from the input file. It then involves four numerical steps in two iteration loops.

The model follows a control volume marching in the fuel flow direction from the control volumes in the inlet area toward the outlet area. In each control volume, the air and fuel gas composition is known from the previous control volume. With the oxygen and hydrogen consumption rates calculated according to Eq. (10), the remaining species content will be calculated, and the gas partial pressure will be balanced to give the new fuel and air composition for the subsequent volume. For the same control volume, the model uses the default internal relation Eq. (3) or another user-specified *I–V* relationship to calculate the current density based on the gas and oxidant temperature, species composition, and cell voltage.

A thermal equilibrium is required for each control volume as shown in Fig. 5(a). Each control volume typically has four neighboring control volumes, and with each one, heat conduction, convection, or radiation takes place. All of these heat transfer modes involve the temperature values of the current control volume and its neighbors. When all mechanisms are considered, including the heat generated from the electrochemistry reaction and the heat transfer to the environment, the equation to be solved is of the form:

$$[A_i] \bullet [T_i] = F_i \quad (23)$$

Here $[A_i]$ is a 1×5 matrix with coefficients for the control volume and its neighbors from thermal calculation, $[T_i]$ is a 5×1 matrix representing the temperature at the center of each control volume, and F_i is the resulting force term for this thermal equilibrium equation. When equations for all control volumes are combined, a matrix equation of temperatures is formed:

$$[A] \bullet [T] = [F] \quad (24)$$

Here $[A]$ is a square matrix with the size of the number of control volumes, $[T]$ is the temperature vector for all control volumes, and $[F]$ is the vector of the force term. Because both $[A]$ and $[F]$ depend on the temperature field for all control volumes, it takes multiple iterations to achieve a solution. The convergence is considered achieved when the temperature difference at every control volume from two consecutive iteration steps is within the user preset tolerance, e.g., 0.1 °C. The calculation of $[T]$ for a given cell voltage distribution constitutes the inner iteration for the model.

For this given cell voltage distribution, the current for each cell in the stack is calculated by integrating the current density along the flow direction. Because all cells are connected in series in the same circuit, each cell must have the same total current. The difference of current in each cell indicates that the cell voltage must be redistributed. This voltage rebalance activity forms the outer loop iteration that converges when the current difference among cells is within the user-specified tolerance, e.g., 1% of the average current. The model reaches a sound solution when convergences for both the inner temperature loop and the outer current–voltage loop are achieved. For a typical tolerance of 0.1 °C for temperature and 1% for current, it takes fewer than 20 iterations on the inner temperature loop and less than 10 iterations on the outer current–voltage loop to converge. The number of iterations needed for the inner loop then decreases as the outer loop converges. The number of

iterations needed for a counter-flow case is approximately double that of a co-flow case.

The multi-physics algorithm was constructed on a given average cell voltage on a multi-cell stack. Several other options were derived by iteratively applying the same algorithm:

- Solve the multi-stack model based on a given average current density.
- Solve the multi-stack model based on a given fuel utilization rate.
- Generate a stack wise *I–V* curve on fixed fuel and air flow rate.
- Generate a stack wise *I–V* curve on fixed fuel and air utilization rate.

For all computational options, the following input information must be specified by the user:

- Cell geometry parameters (number of cells, cell length, width, and height; thickness of interconnect, PEN).
- Fuel and air thermodynamic state (temperature and pressure) and species compositions at the inlet area.
- Boundary conditions (temperatures of the surrounding top, bottom, front, back, and side enclosures including thermal conductivity, emissivity, film coefficients, etc.).
- Operating conditions of either the desired average working voltage of all cells or the desired average current density of all cells is defined based on the designated solution mode.

The model solves the multi-physics system and predicts the following information for the SOFC system:

- Overall SOFC stack performance: total power output, fuel and air utilization, heat loss at each side of the boundary, working voltage for each cell in the stack, working current density.
- Detailed profiles of various thermophysical parameters: temperature, current density, species composition, heat generation at each control volume (fuel, air, PEN, or interconnect).

In addition to the input parameters related to the operating conditions, users also have the flexibility to control the parameters for numerical iteration, such as maximum values for the number of inner loop (temperature) and outer loop (current–voltage) iterations, tolerances for both iterations, and other tuning parameters such as relaxation factors for both temperature and current–voltage iterations. Furthermore, the model offers a restart capability by saving temperature and current values from the previous simulation. This restart feature has proven to be a good feature that will shorten the computation time when small changes are made to input parameters (e.g., during successive calls during a system simulation).

4.1.1. Results and post-processing

Once the convergence criteria are satisfied, the final results are tabulated and output for easy access by the user. Distributions for the current density, temperature, and species concentrations along the path length and voltage through the stack height are output for each cell in the stack. The energy balance is output to indicate the amount of total chemical energy that is converted to useful power, expended as enthalpy increases in the fuel/oxidant flows, or lost to the external environment. The energy balance also assures the user that convergence has been achieved with a small tolerable energy imbalance. Derived stack performance, such as power output, fuel utilization, air utilization, maximum cell temperature, cell temperature difference, gas outlet temperatures, and maximum current density are output for the user. From these sets of data and distribution results, the user can calculate any additional performance metrics of interest for the stack. These post-processing computations have been implemented into an Excel dashboard worksheet to automatically calculate all the stack engineering metrics and plot all the distributions of results using macros. This provides a very simple procedure for the user to perform stack-level engineering calculations to satisfy the design constraints and associated operation criteria.

5. Model verification and validation

A standard set of benchmark cases for SOFC operation and modeling have not been formally adopted by the fuel cell community, but some benchmark cases previously established through collaborative activities at the International Energy Agency (IEA) have emerged as cases of interest. Modeling predictions from a nine-member round-robin test were compared by Achenbach [42] for co-flow, counter-flow, and cross-flow geometries with non-reforming and reforming fuels. Subsequently, these benchmark cases have informally served as test cases for various other researchers who have reported results for their SOFC simulation tools [28,43,59–61]. In contrast to the current state-of-the-art high performance anode-supported SOFCs, the benchmark simulates an electrolyte-supported cell with ceramic interconnect and a low current density of 3000 A m^{-2}. Regardless, the results can still serve as valuable validations for the modeling procedures developed in this study. Therefore, since high fidelity experimental data from well defined stacks has not yet been obtained for public use due to proprietary restrictions, the model predictions from this study are compared to other modeling results in the literature for validation of the approach.

The modeling efforts described above, however, does not seem to have companion cases for multi-cell stacks. Rather, it appears that few multi-cell stack models exist in the literature that fully describe the model basis, inputs, material properties, and results output with sufficient technical detail for replication. One example which is adequately described and will be used here is the five-cell stack studies reported by Burt et al. [62]. Their modeling approach is similar to that taken here and consists of a series of stacked 1D solutions to obtain the 2D variation through the stack cross-section. Their examples evaluated both anode and electrolyte supported cells with parametric studies on the effects of flow maldistribution and radiation heat transfer. Here, four cases using five-cell stacks and uniform flow distributions will be simulated. The anode and electrolyte supported cells will be considered with and without radiation between the cell and interconnect, and comparisons of the predicted temperature profiles will be made.

5.1. Single cell benchmark model

For the IEA cases, the baseline conditions for the model include 3000 A m^{-2} current density, 900 °C inlet gas temperatures, 85% fuel utilization, a stoichiometric air ratio of 7.0, and adiabatic boundary conditions. The IEA electrochemistry model assumes that the anode and cathode concentration polarizations are equal to the electrolyte ohmic polarization for the sake of simplicity. Our quasi-2D model can be compared with co- and counter-flow geometries for each case. For each case, the fuel gas composition is entered as a known parameter, and the IEA electrochemistry model is replicated and implemented through the Lua program interface. The benchmark cases are adiabatic, meaning that no heat is lost to the environment, but the convection coefficient and radiation emissivity for the solid-fluid interfaces are estimated. Output metrics for comparison include voltage, power, efficiency, current density distribution, temperature distribution, and air/fuel outlet temperatures.

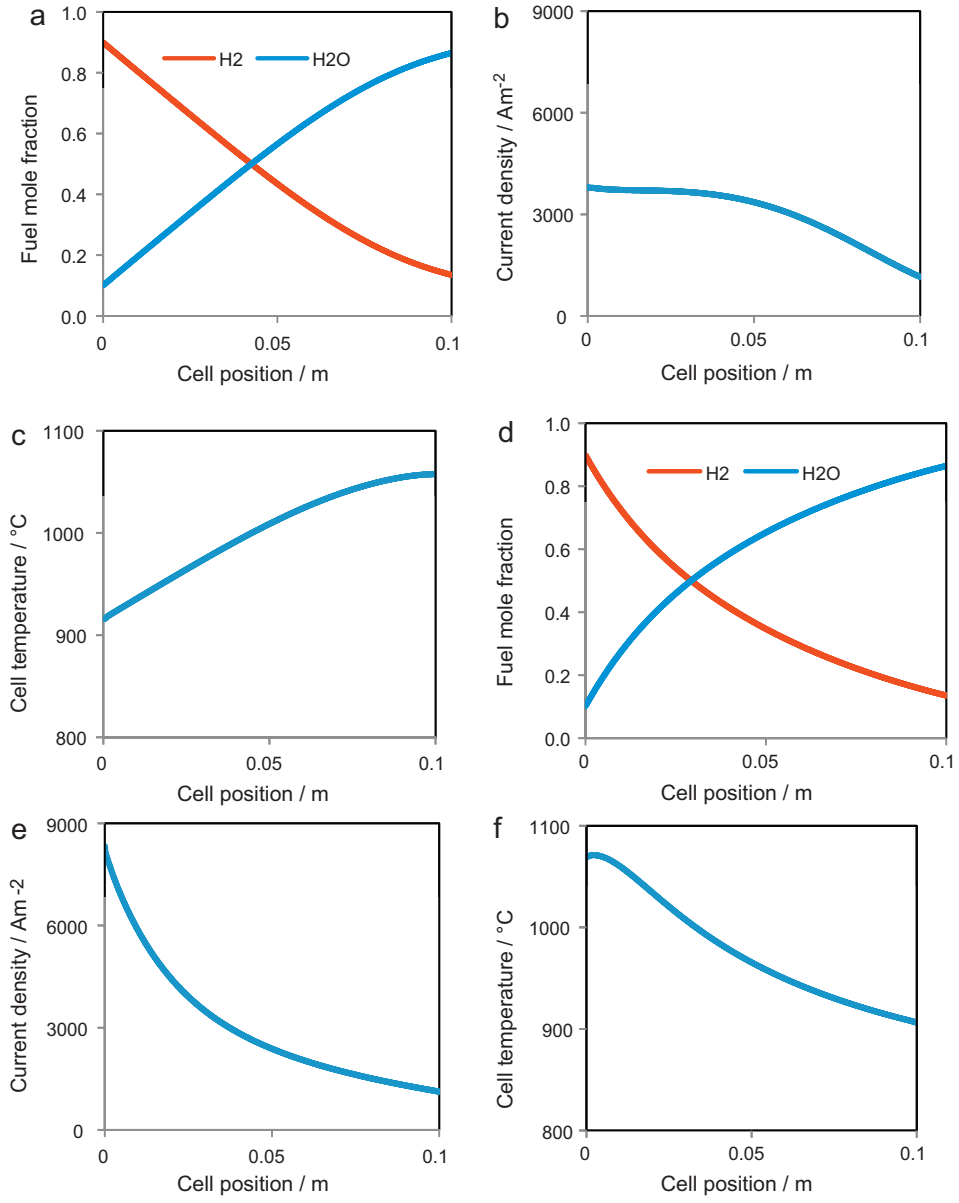

Fig. 6. Simulation results for (a–c) Case 1 co-flow benchmark and (d–f) Case 2 counter-flow benchmark without methane reforming.

5.1.1. Cases 1 and 2: humidified hydrogen fuel

For Case 1 (co-flow) and Case 2 (counter-flow), the fuel is 90% H_2 while the oxidant is standard air with 21% O_2, both with inlet temperatures of 900 °C. The total current density is assigned in the model, and the flow rates are adjusted to achieve the correct utilizations. The resulting distributions for the current density, cell temperature, and fuel composition for the co-flow and counter-flow geometries are shown in Fig. 6. In the co-flow geometry, the current density is relatively uniform over the first half of the cell. This is due to the competing factors along the cell length of improved electrochemical activity due to lower ohmic losses as the temperature gets higher versus the reduced Nernst potential with reduced H_2 concentration due to consumption. Near the outlet, the temperature is high, but the fuel composition is low, resulting in lower current density. For the counter-flow case, the highest cell temperature and the highest H_2 concentration result in much higher current density at the fuel inlet region. The temperature is highest here because of the hot oxidant stream, which removes most of the electrochemical heat from the cell. The current density then drops dramatically along the cell to reach a minimum at the air inlet side where both cell temperature and H_2 concentration are lowest.

5.1.2. Cases 3 and 4: reforming fuel

For Case 3 (co-flow) and Case 4 (counter-flow), the fuel composition is based on a 50% pre-reformed methane composition while the oxidant is again standard air. The resulting input molar composition for the fuel is then 26.26% H_2, 49.34% H_2O, 2.94% CO, 4.36% CO_2, and 17.10% CH_4. In our model, the reforming rate model established by Achenbach and Riensche [52] is used to calculate the composition of CH_4 and other species until full equilibrium is reached. The results for the co-flow and counter-flow geometries are shown in Fig. 7. For the co-flow case, the current density is fairly uniform across the cell. Due to the rapid reformation near the fuel inlet region, the H_2 concentration is high, but the temperature decreases significantly from the endothermic reaction, resulting in slightly reduced current production. The current density increases as the cell becomes hotter downstream. Near the fuel outlet, the low fuel concentration results in a low Nernst value even though the temperature is highest. For counter-flow, the methane still gets reformed quickly near the fuel

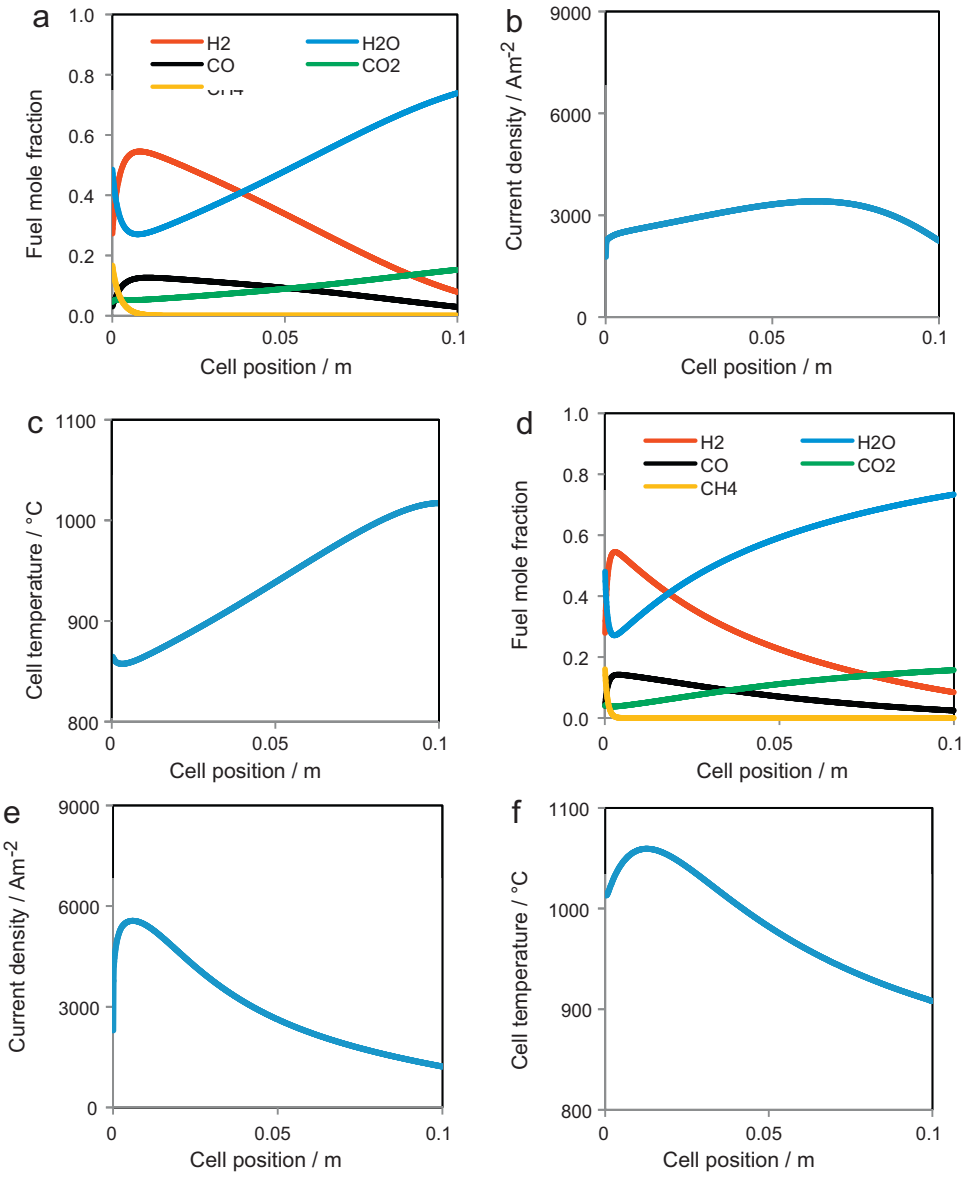

Fig. 7. Simulation results for (a–c) Case 3 co-flow benchmark and (d–f) Case 4 counter-flow benchmark with methane reforming.

inlet side, but the heated air stream compensates for the reformation endotherm, resulting in a higher current density peak from the high temperature and high H_2 concentration. This is similar to the case without reformation, except that the endotherm pushes the location of maximum current density downstream slightly.

5.1.3. Single cell benchmark comparison

The results from the four cases using the present model are shown in comparison to other results from the literature in Fig. 8 [42,60]. The extreme values for these results are compared because the actual distributions for most of these metrics are unavailable, but the comparisons made to available distributions such as Achenbach's temperature data [43] shown in Fig. 9 have been good and the method of comparison is deemed to be acceptable. Overall, these results are generally within the ranges of the other models and are thereby considered to be an acceptable match, especially with the approximations utilized to simulate the rib geometry. The electrical performance results were very comparable. The model voltages were close to the mean value of the reference predictions, while the minimum and maximum current densities fell within the range of the literature values. This suggests that the overall current density distributions and fuel distributions across the cell are suitably captured by this model. The temperature results compared reasonably well to the reference results also, although there were some small discrepancies. The maximum cell temperatures with the reforming fuel were slightly lower than the reference range by 4–17 °C for the co-flow configuration (Case 3) and 3–30 °C for the counter-flow configuration (Case 4). Also, the fuel outlet temperature for the co-flow configuration (Case 3) was 4–9 °C lower than the reference range and the air outlet temperature for the counter-flow configuration (Case 4) was 2–12 °C lower than the reference range. The exact reasons for these discrepancies remain difficult to diagnose, but can possibly be attributed to the following factors: (1) the shape of the current density profile determined with the reforming rate equation, (2) the convective transport properties, and/or (3) the model mesh density. The rapid methane reformation at the fuel inlet side results in steep gradients of the hydrogen species concentration. The coupled current density and thermal profile will then depend on the heat removed by the thermal transport mechanisms. Since the assumptions and temperature dependence for the convective film coefficients are also unknown, the convective heat transfer to the gas streams may be slightly different from

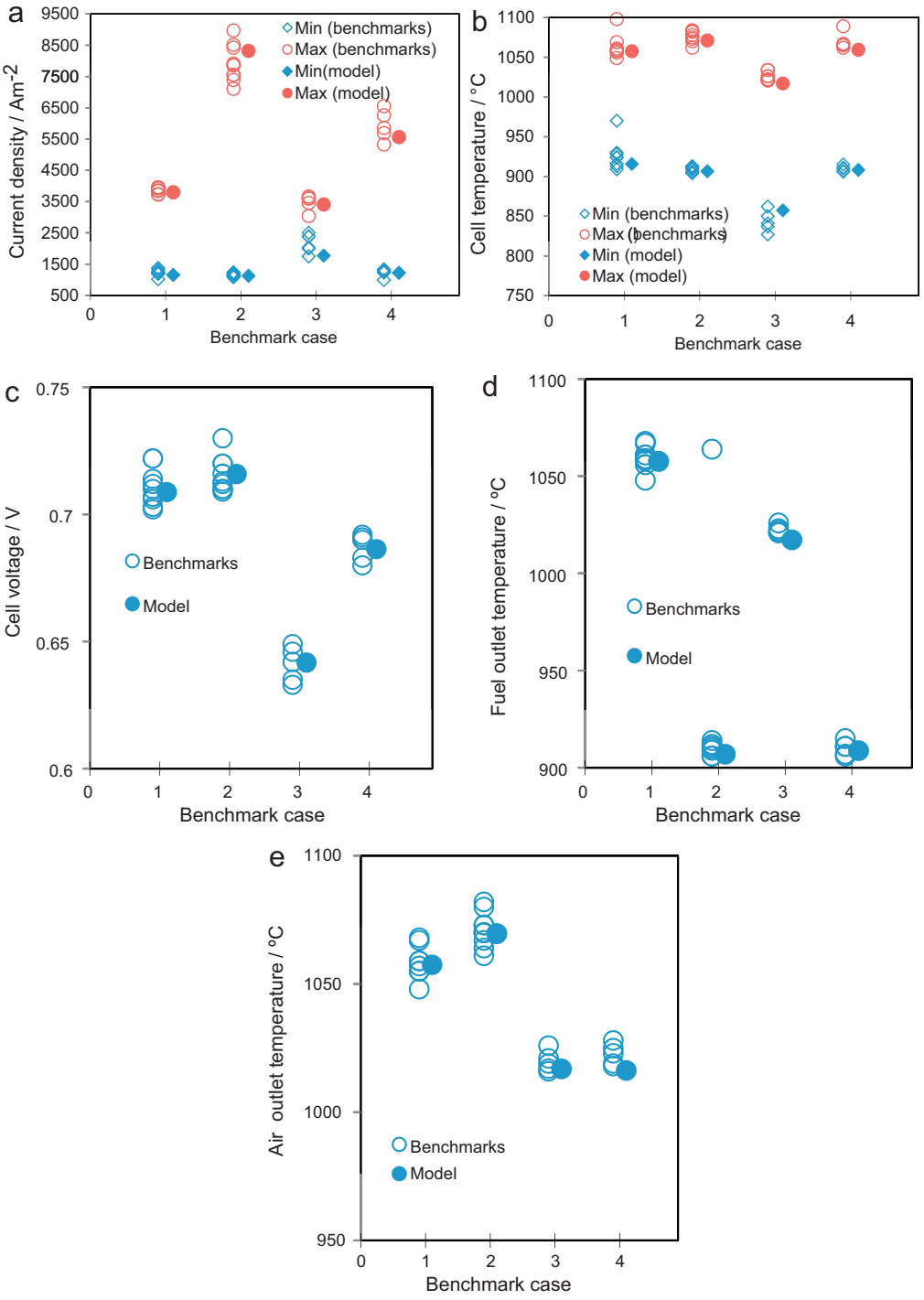

Fig. 8. Simulation results for (a) minimum/maximum current density, (b) minimum/maximum cell temperature, (c) voltage, (d) fuel outlet temperature, and (e) air outlet temperature for benchmark Cases 1–4 with comparisons to literature results.

the reference models. Furthermore, a model mesh density of 1000 increments was used for these benchmark cases, while the mesh resolution of the reference cases is unknown. Mesh resolution differences could be important for accurate capture of peak values near the edge of the model domain such as fuel and air outlet temperatures. In Case 2 for example, the fuel temperature changes significantly from the 900 °C inlet value within the first volume increment (+16 °C) and accordingly affects the reformation rate, while in Case 3 the peak cell temperature occurs at the air outlet edge. Therefore, despite the lack of the necessary detailed assumptions/inputs to replicate the original benchmark cases, the results still compare reasonably well overall and validate the use of this code as an engineering stack-level simulation tool.

5.2. Multi-cell stack example model

For the models presented in Burt et al. [62], a five-cell stack was used consisting of 900 cm^2 co-flow cell with the 10 cm short dimension along the flow direction. The inlet fuel was 900 °C wet hydrogen with 3 mol% water, while the inlet oxidant was 900 °C standard air. Current levels of 50–650 A were evaluated, but constant fuel and air flow rates were used so that utilizations varied

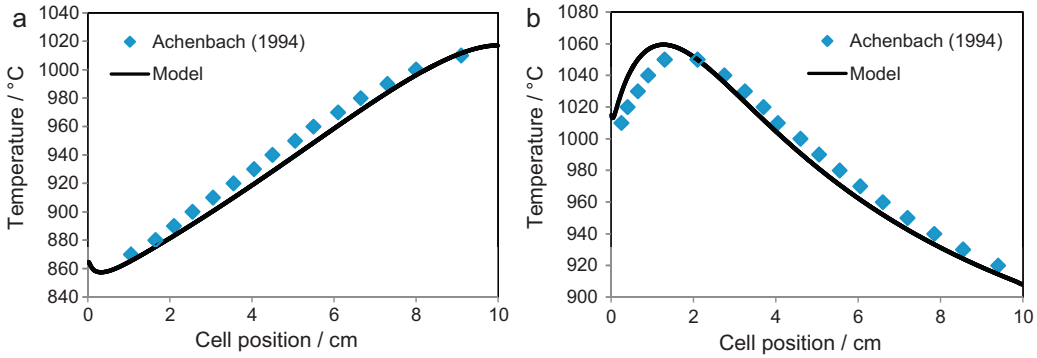

Fig. 9. Comparison of the temperature distribution results for the (a) co-flow and (b) counter-flow cases with reforming fuel.

for different current densities. The cell was assumed to be adiabatic with no heat loss to the external environment. The relations for the electrochemistry model consisting of the Nernst voltage minus ohmic, activation, and concentration polarizations were coded in the user-defined Lua interface. Output metrics for comparison include voltage, power, efficiency, current density distribution, temperature distribution, and air/fuel outlet temperatures. In this paper, the simulated *I–V* relationship for the electrolyte-supported stack and the temperature distributions for the top and bottom cells of the five-cell stack are used for comparisons.

While nearly all of the necessary model parameters (e.g., dimensions, thicknesses, gap heights, flow parameters, EC parameters, etc.) for comparison were available in the associated paper and Refs. [63–65], detailed analyses found three parameters that required additional assumptions for input to the models. First, the empirical Nusselt number correlation used to compute the convective coefficients for heat removal by the fuel and oxidant flows was not provided. Here, convection coefficients were calculated from an assumed Nusselt number of 8.23 corresponding to fully developed laminar flow through an infinitely wide rectangular cross-section with uniform heat flux [66]. Second, the stated contact and separator plate areal resistance was 0.1 $\Omega\,cm^{-2}$, which appears to be a typographic error since it yields an unrealistic 90 V ohmic loss for the 900 cm^2 cell. Rather we assumed a volume resistivity of 0.1 $\Omega\,cm^{-3}$ which yields a more reasonable 0.18 V ohmic loss for the 0.002 m thick interconnect plate. Third, the stated limiting current was 4000 A m^{-2}, but the *I–V* curve is nearly linear and extends beyond current densities of 6666 A m^{-2}. It was therefore assumed that no concentration losses were present. The remaining model parameters were used as stated in the references. The thermal conductivity of the cell and interconnect were set to zero since the literature cases did not include the effects of in-plane conductive heat transfer.

5.2.1. Cases 5 and 6: electrolyte-supported cell

These models correspond to the solutions for an electrolyte-supported cell solved with (Case 5) and without (Case 6) the effect of thermal radiation between the cell and interconnect. The electrolyte-supported model consisted of 180 μm electrolyte with 50 μm anode and cathode electrodes. The cases for comparison were performed for a current of 300 A (3333 A m^{-2}), fuel utilization of ~38%, and air utilization of ~10%. As a preliminary test, the model was evaluated with the low air flow rate (1.09e−3 kg s^{-1}) for current densities of 575–6666 A m^{-2} to validate the implementation of the electrochemical model. The results for the predicted stack *I–V* curve and the reported reference values are shown in Fig. 10 for comparison. The predicted values are slightly lower than the reference values with the largest difference of −3.7% at the maximum current density. As this depends on the temperature distributions through all of the cells, the difference is attributed to prediction of a lower stack temperature distribution as discussed below. The electrochemical model is assumed to correctly capture the *I–V* performance and therefore validates the assumption on the reported volumetric resistivity of the interconnect.

5.2.2. Cases 7 and 8: anode-supported cell

These models correspond to the solutions for an anode-supported cell solved with (Case 7) and without (Case 8) the effect of thermal radiation between the cell and interconnect. The anode-supported cell has 1000 μm anode with 10 μm electrolyte and 25 μm cathode. The ohmic heating will be much less in this cell as the anode resistivity is about 10,000× less at 1000 °C. The cases for comparison were performed for a current level of 600 A (6666 A m^{-2}), fuel utilization of ~76%, and air utilization of ~20%.

5.2.3. Multi-cell stack example comparisons

The temperature distributions for the multi-cell example cases are shown in Figs. 11 and 12 with the reported reference results. The cell temperature profile along the flow direction is plotted for the top and bottom cells of the stack. Since the fuel and oxidant gases are heated as they flow across the cell due to the electrochemical activity in the cell, the cell is coolest near the inlet side and hottest at the outlet side as expected for a co-flow configuration. Due to the different convective heat removal capacity between the fuel and oxidant streams, an asymmetric temperature profile develops between the cells in the stack, particularly with an adiabatic boundary condition. The low utilization oxidant removes more heat, so a cell at the periphery of the stack not sharing any air flow channel with adjacent cell will be cooler. This is observed in the results for both the anode-supported and the electrolyte-supported where

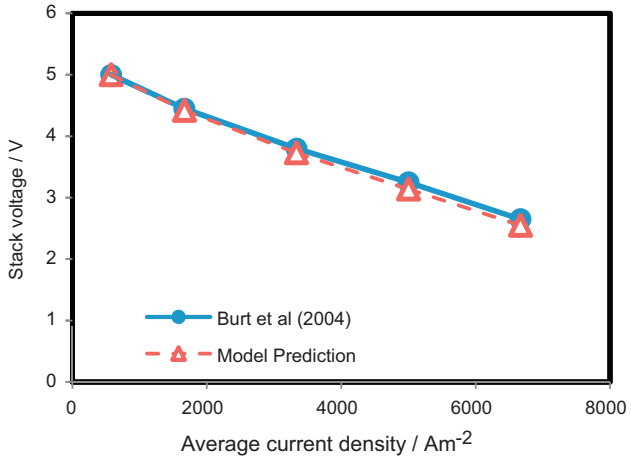

Fig. 10. Comparison of reference and predicted current–voltage relationship for the five-cell electrolyte-supported stack without radiation.

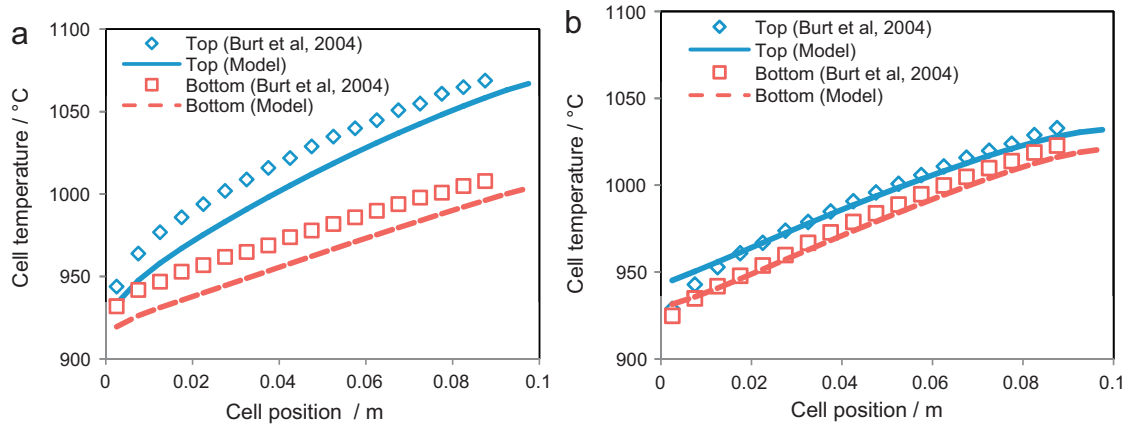

Fig. 11. Comparison of the reference and predicted cell temperature distributions for the top and bottom cells of the five-cell electrolyte-supported stack (a) without and (b) with radiation heat transfer between cells.

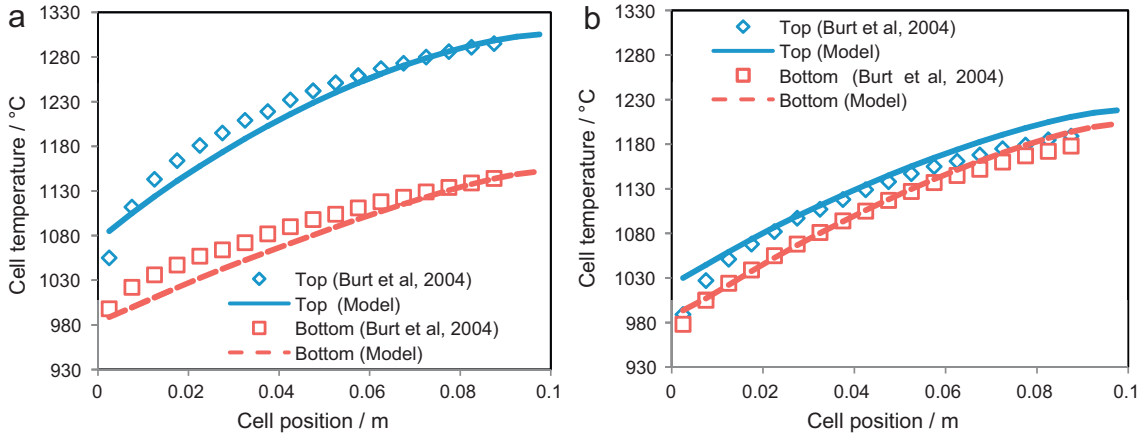

Fig. 12. Comparison of the reference and predicted cell temperature distributions for the top and bottom cells of the five-cell anode-supported stack (a) without and (b) with radiation heat transfer between cells.

the top cell is always hotter. This effect is amplified when radiation between cells is neglected. Without radiation, convection between the solid and fluid domains is the only heat transfer mechanism from cell to cell. With radiation, dual heat transfer mechanisms reduce the temperature difference between cells and drive the stack to a more isothermal condition. This was demonstrated for both cell support types and indicates the importance of radiation for reducing thermal gradients.

Comparison of the results shows that the trends are well captured but some important differences between the temperature fields remain. Most noticeably, the prediction for the electrolyte-supported cell without radiation is low overall. Other differences include a generally higher prediction for the anode-supported cell with radiation and a different curve shape for the anode-supported cell without radiation. The differences can be attributed primarily to the assumptions on the convective heat transfer. First, because the empirical Nusselt number correlation is not known, the use of the relation for a parallel plate enclosure will introduce some difference. Second, the model in its current state assumes only a single value for convection coefficient along the flow domain and neglects any temperature effects for both the oxidant and fuel. Furthermore, the convective heat transfer coefficient for the fuel may also depend on the composition, as the thermal conductivity of hydrogen is 4× higher than steam at 1200 K (528e−3 and 125e−3 $W K^{-1} m^{-1}$, respectively). The convection coefficient of the mixture will vary from the fuel rich inlet to the fuel depleted outlet. The model here used a single value based on the average cell temperature and average composition, so this is assumed to be the primary assumption responsible for the difference between the results predictions. Because lower temperature yields higher Ohmic loss, a slightly lower *I–V* response is predicted as shown in Fig. 10. Overall, reasonably good model comparisons have been achieved.

6. Simulation results for multi-cell stacks

The SOFC-MP modeling tool was next used to evaluate a large multi-cell stack characteristic of the modern stacks currently under development in the SECA program. This model served as a baseline for comparison with other models that demonstrate the features of this tool. Specifically, the tool was used to evaluate the cooling benefits of a reforming fuel. The model also has the capability for simulating the cell-to-cell variations with different stack parameters. This feature is useful for identifying the sensitivity of stack performance to various off-normal conditions, so that researchers can maximize their understanding of stack performance in actual tests and experiments. This capability for cell-to-cell variation which is absent in most 0D and 1D models and proven computationally expensive for 3D models can be accomplished fairly easily in the SOFC-MP 2D model. The model is currently capable of simulating the following cell-to-cell variations, e.g.:

- Thick plates in middle of stack (e.g., for thermocouple measurements, load frame).
- Different flow rates in cells (e.g., blockage, leak, by-pass).

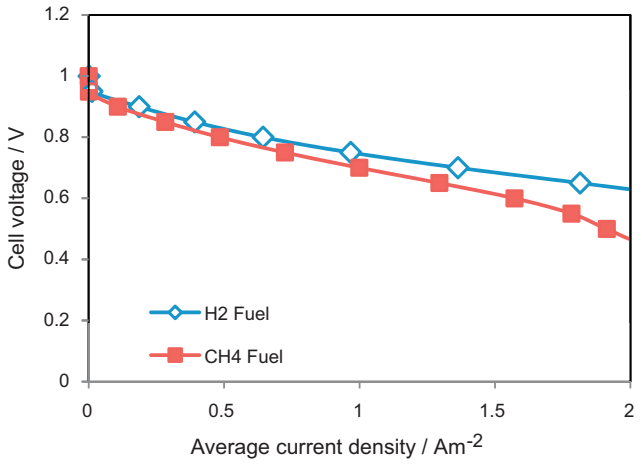

Fig. 13. High performance *I–V* response for the baseline 96-cell stack model with both hydrogen and reforming fuels.

- Different *I–V* performance of cells.
- Short current in cells.
- Partial contact in cells.

As examples in this paper, the influence of an instrumented plate introduced to the stack for temperature measurements and a gas flow restriction is assessed. In this section, the stack-wise metric for simulation of the 96-cell stack is obtained for comparison to several off-normal conditions to demonstrate the capabilities of SOFC-MP 2D model.

6.1. 96-Cell baseline stack

SOFC manufactures have made great technical strides in the pursuit of larger, more powerful stacks. Developers within the SECA program are currently testing stack towers with normal power outputs of 25 kW or larger [67]. For these stack towers consisting of nearly 200 planar cells, variation of temperature and electrical performance is expected along the stack height. These variations must be understood to determine appropriate operating conditions that prevent high temperatures, high current densities, high local fuel utilizations, or other behaviors that can lead to performance degradation. In this section, the SOFC-MP 2D model will be used to evaluate flow–thermal–electrochemical performance of a tall stack characteristic of modern designs while still providing resolution of the field variation across cells and along the stack height. The simulations are based on a hypothetical model due to the lack of detailed published data on tall SOFC stacks.

The baseline stack consisted of a large 625 cm^2 active area cell (25 cm × 25 cm) operated at an average current density of 0.5 A cm^{-2} in a 96-cell stack to provide a total power output of 25.5 kW. The temperature of the inlet gases was assumed to increase along the stack height from 700 °C for the bottom cell to 730 °C at the top cell of the stack. The stack was assumed to be in a 750 °C furnace with external stack heat loss via radiation (emissivity of 0.7) and convection (free convection coefficients of 0.3–1.5 W m^{-2} K). The electrochemistry parameters were selected to give a very high performing cell characteristic of the state-of-art for peak power conditions of SECA SOFCs [38,39,58], and the *I–V* curve is shown in Fig. 13. The fuel was wet hydrogen with 3% water, and the stack was run at 65% fuel utilization and 15% air utilization.

The predicted performance was an average cell voltage of 0.852 V and total power of 25.5 kW. Thermal performance indicated a mean cell temperature of 793 °C with minimum and maximum

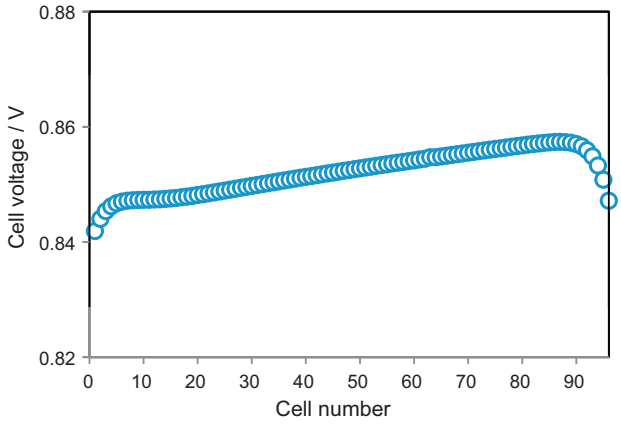

Fig. 14. Cell voltage profile for the 96-cell stack operating with wet hydrogen fuel.

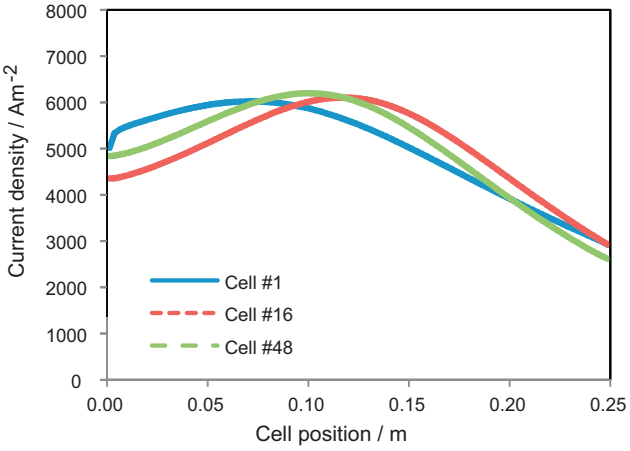

Fig. 15. Current density distribution along various cells of the 96-cell stack operating with wet hydrogen fuel.

values of 709 °C and 848 °C, respectively. Results for the voltage profile along the stack height, current density across various cells, cell peak temperatures, cell temperature across various cells, and cell temperature difference is shown in Figs. 14–18, respectively. The profile in Fig. 14 showed that the voltage generally increased along the stack height with a total variation of 0.015 V, while the top and bottom cells showed a local voltage decrease. This performance is due to the improved electrochemical performance for

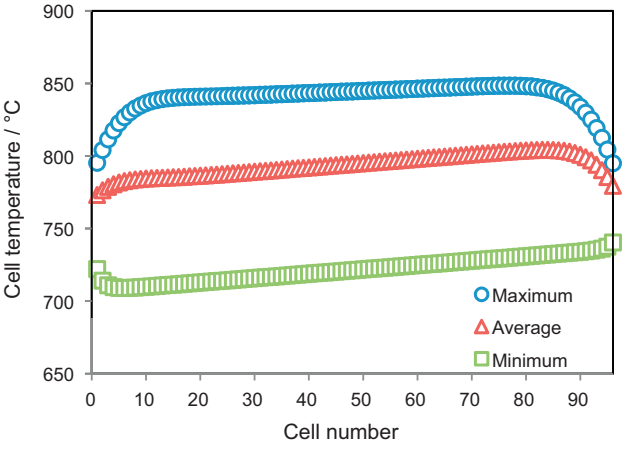

Fig. 16. Profile of cell minimum, maximum, and average cell temperatures for the 96-cell stack operating with wet hydrogen fuel.

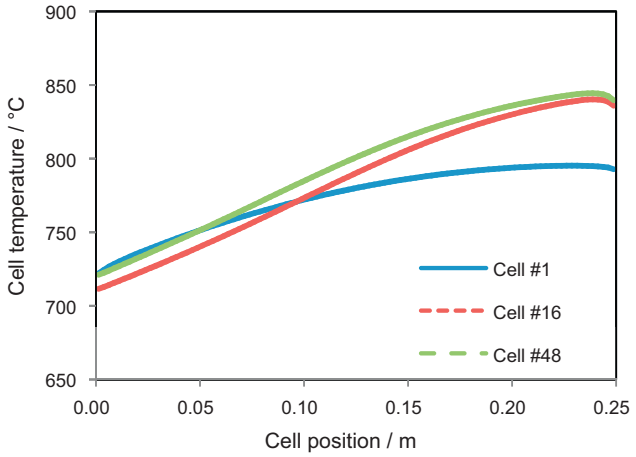

Fig. 17. Temperature distribution along various cells for the 96-cell stack operating with wet hydrogen fuel.

regions with higher temperature. The temperature profile (Fig. 16) shows that the cells are generally hotter near the top of the stack due to the inlet gas flow temperatures, but heat transfer with the furnace affects the temperatures for the top and bottom cells by driving them toward 750 °C. The current density for the top, bottom, and middle cells are shown in Fig. 15. Cells higher in the stack tend to consolidate the current near the fuel inlet with the hotter inflow gases. However, the minimum temperature of the top and bottom cells (which occurs at the fuel inlet as shown in Fig. 17) increases due to furnace heating so that these end cells show the most current consolidation at the leading edge (Fig. 15). This will be important to stack designs since high current densities are likely to be more conducive to various degradation processes. Also, the highest cell temperature difference of about 139 °C occurred in cell #15 (Fig. 18). The cell temperature difference is also an important metric for design since greater thermal strain variation can lead to unwanted cell warpage and structural stresses.

6.1.1. Effect of reforming

The use of on-cell reforming of methane is advantageous for SOFCs because the endothermic reaction removes heat and may be beneficial in thermal management for cells with large area. The baseline model was run at the same current density with a 50% on-cell reforming fuel consisting of a molar composition of 32.4% H_2, 33.3% H_2O, 4.9% CO, 6.1% CO_2, 11.0% CH_4 and 12.4% N_2. The reforming rate following the expression of Achenbach was used,

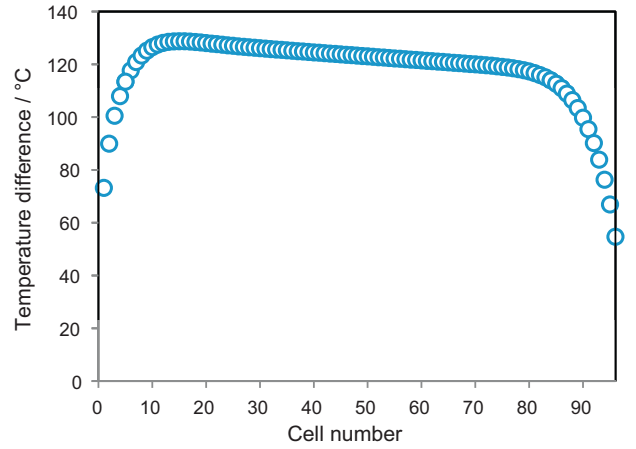

Fig. 18. Cell temperature difference profile for the 96-cell stack operating with wet hydrogen fuel.

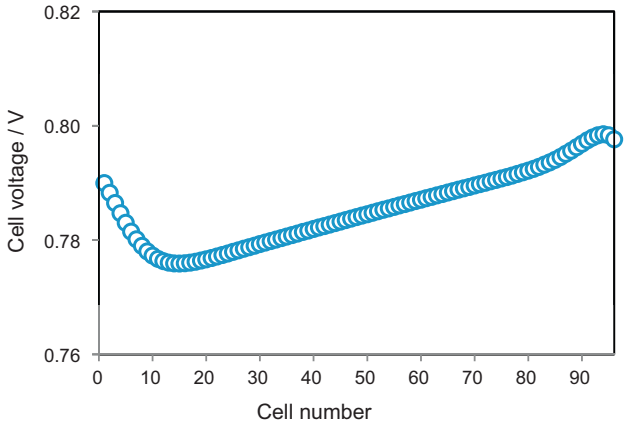

Fig. 19. Voltage profile for the 96-cell with reforming fuel.

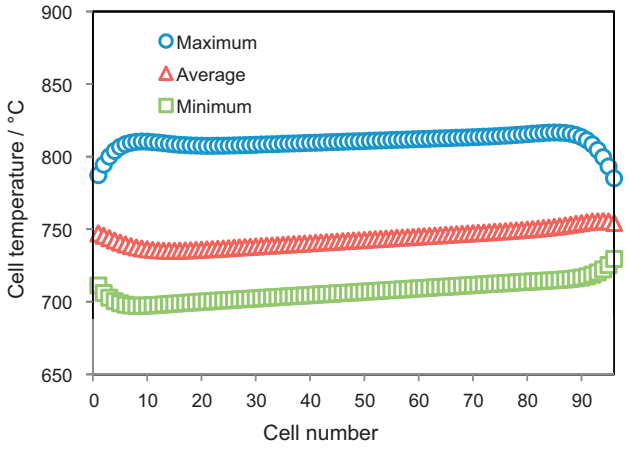

Fig. 20. Profile of the minimum, maximum, and average cell temperatures for the 96-cell with reforming fuel.

and the CH_4 was fully reformed for this case. The total power output decreased 7.5–23.6 kW due to the lower Nernst potential which resulted in an average cell voltage of 0.785 V. The voltage profile in Fig. 19 shows that the lowest voltage was observed near cell #15. This was again explained by the temperature profile and the periphery boundary condition effects which lead to the lowest average cell temperature to occur in this part of the stack (Fig. 20). The current density distribution (Fig. 21) shows the highest values near the cell

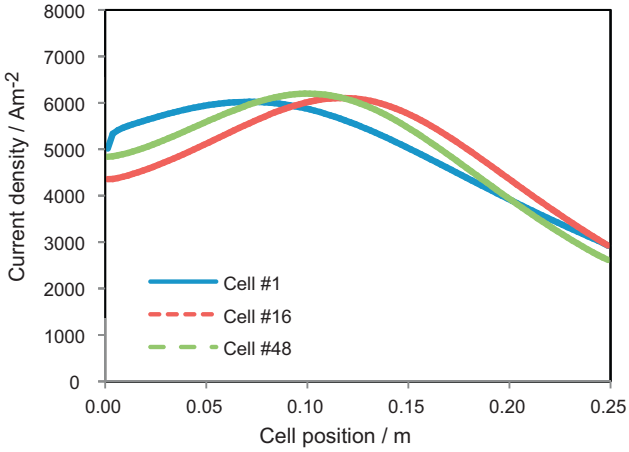

Fig. 21. Current density distribution for various cells of the 96-cell stack with reforming fuel.

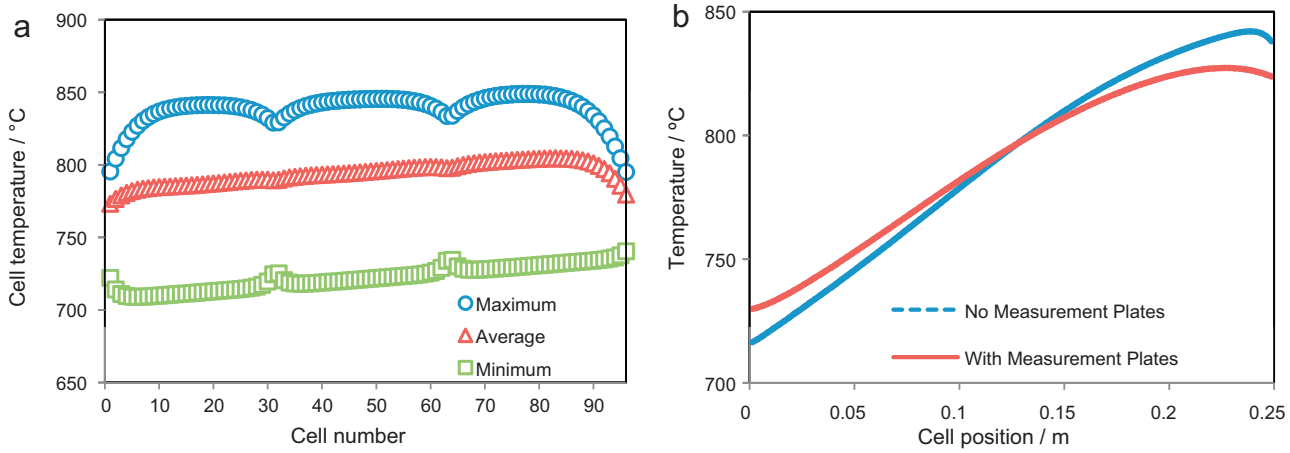

Fig. 22. Demonstration of the effect of using thicker interconnect plates for cells #30 and #60 on the temperature (a) peak values and (b) distribution.

outlet due to the endothermic reaction near the fuel inlet side. The peak current density in the stack was increased 6–0.69 A cm^{-2} compared to the peak value of 0.65 A cm^{-2} in the H_2 stack. The benefits of the reforming fuel were observed when the average cell temperature was reduced from 793 °C to 743 °C, the maximum temperature reduced 31 °C from 848 °C to 817 °C, and the maximum cell temperature difference reduced 20 °C from 139 °C to 119 °C. Models such as these can help the stack designer with the judicious use of reforming to manage trade-offs between high temperatures that can lead to material degradation, high temperature gradients that can create thermal-mechanical stresses, and high current densities that can lead to degradation.

6.1.2. Effect of measurement plates

Fuel cell developers have sought ways to obtain real time measurement of the stack thermal state during testing to assess the design margin between maximum operating temperature and temperature limits for material stability. This is critical in achieving an acceptable long-term power degradation rate by preventing various degradation mechanisms that are thermally activated (e.g., scale growth, oxidation, interfacial reactions, species volatilization, etc.). Evaluation of temperature within the stack is difficult because precise sensor placement will likely require an undesirable penetration through the hermetic seals in the stack, and multiple sensor placements within manifolds and cells may adversely affect the gas flow characteristics, and any instrumentation must ensure it does not provide a short circuit electrical path. One effective alternative is to use an instrumented plate which consists of numerous embedded thermocouples in a structure patterned as the cell manifold design which can then be introduced and sealed between any two cells in a tall stack. The numerous sensors can then provide enough resolution to characterize the actual temperature profile across the cell.

However, this approach could potentially suffer from the so-called "observer effect" where the measurement method strongly influences the data being measured. The thicker instrumented plate will likely provide an enhanced in-plane thermal conduction compared to the thin interconnect which will affect the measured temperature field. In this example, the plate thickness of cells #32 and cell #64 is increased from the nominal value of 0.5–12 mm, simulating the introduction of two relatively thick measurement plates. Fig. 22(a) shows the maximum, minimum, and average temperature distribution of all cells in the stack, while Fig. 22(b) plots the temperature distribution in the flow direction for measured cell #30 and its neighbor cell #32. Comparison of Fig. 22 to the nominal case in Fig. 16 shows that while the average temperature of the cells is nearly the same in the neighborhood of the measurement plates, the minimum and maximum temperatures of these cells are greatly affected. For the thicker plates, the improved thermal conductivity path spreads heat better to smooth temperature gradients in the cell. The minimum temperature at the inlet is higher while the maximum temperature is lower. This results in the designer underestimating the temperature difference by 18% and the maximum temperature by 13 °C. This underestimation is highly undesirable since it may mislead the designer to think that the stack is operating within the desired temperature range while, in fact, it is not. Similar thermal effects are expected from the use of large manifold or load frame structures in tall stack towers. Modeling tools such as this can help the designer to understand the impact of these structures on the thermal profile in the stack.

6.1.3. Effect of flow maldistribution

The cells in the SOFC system are generally designed to run at an optimal condition with uniform flow rates in each cell to achieve the desired fuel and air utilization. However, certain design and assembly factors can adversely affect gas flows (e.g., leak through poor seals, flow restriction/blockage due to sealant overflow, bypass of fuel around the cell) and downgrade the cell performance. The SOFC-MP 2D model can be used to evaluate how localized downgraded cells will impact the overall stack performance. As an example case, cells #32 and #64 of the 96-cell stack are assumed to have flow restrictions, i.e., cell #32 has a 25% reduction in fuel flow rate and cell #64 has a 50% reduction in oxidant flow rate.

The results show that the fuel flow restriction has the most significant effect on the performance. The reduced fuel flow increases the fuel utilization on cell #32 from 65% in the baseline case to 87%. This reduces the H_2 concentration over the cell which reduces the Nernst potential, makes cell #32 less efficient, and drops its voltage by 5% from the baseline 0.85–0.81 V. The current then concentrates near the fuel-rich inlet with a 21% increase in peak current density from 0.61 A cm^{-2} in the baseline case to 0.74 A cm^{-2} (Fig. 23a). The higher heat load then increases the average local cell temperature by 9 °C (+1.1%) but the peak cell temperature only increases by 5 °C (+0.6%) as shown in Fig. 23b. The flow restriction on the air had a much less impact since the air utilization is much lower. The voltage decreased slightly by 0.5 V from the adjacent cells, but the effect of air restriction on the cell temperature was almost negligible.

6.1.4. Effect of electrochemical performance

The variation of cell performance depends not only on the operating conditions but also on the quality control of the cell fabrication

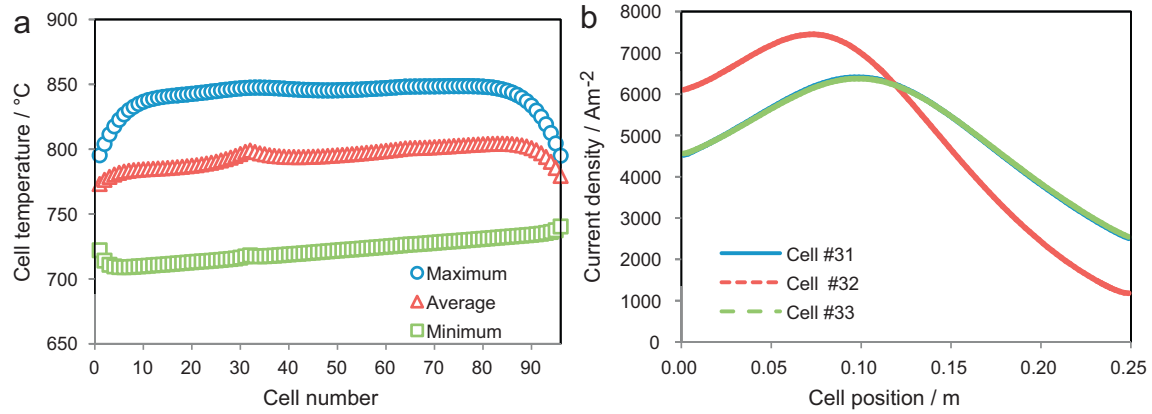

Fig. 23. Contours of the (a) minimum, maximum, and mean cell temperatures and (b) current density distribution for the 96-cell stack with reduced fuel (#32) and air (#64) flow rates.

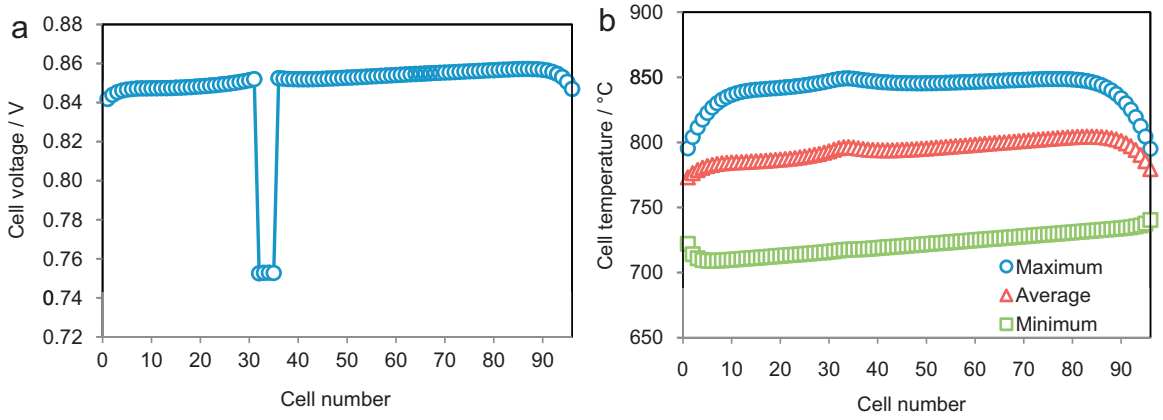

Fig. 24. Voltage and temperature distribution for 96-cell stack with four poor performing cells: #32, #33.

and assembly processes. Cells with inherently different electrochemical properties may be present in one single assembled stack. Alternatively, undesirable degradation processes may occur within a tested stack that cause local voltage drops. The modeling tool can simulate the different electrochemical performance of individual cells to simulate the effect of underperforming cells on the stack response. This is important as it provides the designer with the maximum amount of information in a stack experiment where voltage degradation has occurred. For this example, four cells #32–35 were assumed to have added resistance resulting in an additional 0.1 V voltage loss.

Fig. 24(a) shows the stack-wise voltage distribution and (b) shows the temperature distribution changes caused by the downgraded cells. The stack power output correspondingly decreased about 0.35%, but the primary influence on the stack was local temperature increase in the cells. The added ohmic heat increased the local average cell temperature by ~6 °C, the peak cell temperature by ~7 °C, and the cell temperature difference by ~6 °C. Depending on the severity of voltage degradation and the number of cells affected, the impact on the stack temperatures may be important for certain components' temperature limits.

7. Model performance and scalability

The total number of control volumes in the system is $(N_{\text{cells}} \times 4 + 1)N_x \rightarrow 4N_{\text{cells}}N_x$, which is proportional to the number of cells N_{cells} and the number of increments in the axial direction N_x. A large portion of the computational time is spent on solving the matrix for temperature. The computational time spent on the matrix solver chosen for this sparsely populated thermal matrix is slightly more than linear to the total unknowns. The total iterations from the two loop iterations (temperature field and current) depends more on the multi-physics characteristics of the model rather than the total number of control volumes. Therefore, the total computation time is proportional to the number of cells and the number of mesh increments. Naturally, the computational time also depends on the convergence tolerance set for the temperature field and the current.

It is shown that for all benchmark cases, mesh size convergence is usually achieved around $N_x = 200$, regardless of the number of cells or the flow direction. As a result, the SOFC-MP model can easily manage the simulation of a large system, e.g., a system with 100 cells and 500 increments. For co-flow, a system with 100 cells and 500 increments requires about 8 min on a 2 GHz Windows XP server without the restart capability using the previous saved data. Because the air flows in the opposite direction, the thermal properties of the air will not be known from the previous control volume; they will be assigned values from previous iteration step instead. As a result, it takes more iteration steps to achieve a stable solution, and the computational time on a counter-flow system is usually higher, e.g., about 20 min for the same configuration, but still manageable.

The computational effort for SOFC-MP simulation is much greater if the average current density solution mode is specified instead because multiple simulations for the trial average voltage will be run. A typical simulation for target current density runs about 10 times the equivalent simulation on voltage, but is still manageable.

8. Conclusions

A quasi-2D multi-physics finite volume SOFC model was successfully developed for simulating steady-state co-flow and counter-flow multi-cell SOFC stack systems. Species conservation, energy conservation equations, and electrochemical *I–V* models were solved in the model to provide the overall system performance metrics along with the distributions of temperature, species concentrations, current density, and voltage through the stack. The predicted results from the model compared very well with single cell benchmark cases using different fuel compositions and flow geometries. The results for five-cell co-flow and counter-flow stacks with and without internal radiation also compared reasonably well with published simulation results. The authors recommend that a comprehensive suite of well defined benchmarks should be established by the fuel cell community to support SOFC model validation activities and include potential variations for cell size, stack size, external heat loss, on-cell reforming, and manifold structures.

Simulation results have been presented for a 25 kW multi-cell stack to illustrate the model capability on handling cell-to-cell variations and user defined electrochemistry. On-cell reforming was shown to beneficially reduce the stack temperature and temperature gradient at the expense of a small power loss. The presence of thick plates in the stack for thermocouple placement was shown to dramatically affect the stack's measured peak temperature and temperature difference, indicating that designers must included these features to accurately characterizes multi-cell stack experiments. The influence of reduced fuel/oxidant flow and cell electrochemical performance on the maximum current density and cell temperatures was also demonstrated. Future study will include a more comprehensive parametric study on large cell stacks using the cell-to-cell variation feature to characterize stack performance for realistic performance variations.

Acknowledgements

The work summarized in this paper was funded as part of the Solid-State Energy Conversion Alliance Core Technology Program by the U.S. Department of Energy's National Energy Technology Laboratory. PNNL is operated by Battelle for the U.S. Department of Energy under Contract DE-AC05-76RL01830.

References

[1] N.Q. Minh, J. Am. Ceram. Soc. 76 (3) (1993) 563–588.
[2] H.H. Mobius, J. Solid State Electrochem. 1 (1997) 2–16.
[3] M.L. Perry, T.F. Fuller, J. Electrochem. Soc. 149 (2002) S59–S67.
[4] W.A. Surdoval, S.C. Singhal, G.L. McVay, in: H. Yokokawa, S.C. Singhal (Eds.), Proceedings of the 7th Int. Symp. on Solid Oxide Fuel Cells, PV 2001-16, The Electrochemical Society Pennington, NJ, Tsukuba Ibaraki, Japan, 2001, pp. 53–62.
[5] M.C. Williams, J.P. Strakey, S.C. Singhal, J. Power Sources 131 (2004) 79–85.
[6] M.C. Williams, J.P. Strakey, W. Surdoval, J. Power Sources 159 (2006) 1241–1247.
[7] O. Yamamoto, Electrochim. Acta 45 (2000) 2423–2435.
[8] S.P.S. Badwal, K. Foger, Ceram. Int. 22 (1996) 257–265.
[9] J.P.P. Huijsmans, Curr. Opin. Solid State Mater. Sci. 5 (2001) 317–323.
[10] S.H. Chan, K.A. Khor, Z.T. Xia, J. Power Sources 93 (2001) 130–140.
[11] A.V. Virkar, J. Chen, C.W. Tanner, J. Kim, Solid State Ionics 131 (2000) 189–198.
[12] S. Campanari, P. Iora, Fuel Cells 5 (2005) 34–51.
[13] M.A. Khaleel, Z. Lin, P. Singh, W. Surdoval, D. Collins, J. Power Sources 130 (2004) 136–148.
[14] P. Costamagna, K. Honegger, J. Electrochem. Soc. 145 (1998) 3995–4007.
[15] M. Iwata, et al., Solid State Ionics 132 (2000) 297–308.
[16] E. Boudghene Stambouli, E. Traversa, Renew. Sustain. Energy Rev. 6 (2002) 433–455.
[17] R. Bove, S. Ubertini, J. Power Sources 9 (15) (2006) 543–559.
[18] H. Yakabe, T. Ogiwara, M. Hishinuam, I. Yasuda, J. Power Sources 102 (2001) 144–154.
[19] P. Aguiar, C.S. Adjiman, N.P. Brandon, J. Power Sources 138 (2004) 120–136.
[20] A. Salogni, P. Colonna, Modeling of solid oxide fuel cells for dynamic simulations of integrated systems, Appl. Therm. Eng. 30 (2010) 464–477.
[21] C.-Y. Wang, Chem. Rev. 104 (2004) 4727–4766.
[22] S. Kakac, A. Pramuanjaroenkij, X.Y. Zhou, Int. J. Hydrogen Energy 32 (2007) 761–786.
[23] C.O. Colpan, I. Dincer, F. Hamdullahpur, Int. J. Energy Res. 32 (2008) 336–355.
[24] D. Bhattacharyya, R. Rengaswamy, Ind. Eng. Chem. Res. 48 (2009) 6068–6086.
[25] R.J. Kee, H. Zhu, D.G. Goodwin, Proc. Combus. Inst. 30 (2005) 2379–2404.
[26] R. Bove, P. Lunghi, N.M. Sammes, Int. J. Hydrogen Energy 30 (2005) 181–187.
[27] R. Bove, P. Lunghi, N.M. Sammes, Int. J. Hydrogen Energy 30 (2005) 189–200.
[28] M. Li, J.D. Powers, J. Brouwer, J. Fuel Cell Sci. Technol. 7 (2010).
[29] K.P. Recknagle, R.E. Williford, L.A. Chick, et al., J. Power Sources 113 (2003) 109–114.
[30] N.M. Sammes, Y. Du, R. Bove, J. Power Sources 145 (2005) 428.
[31] S. Campanari, P. Iora, J. Power Sources 132 (2004) 113–126.
[32] K. Kendall, M. Palin, J. Power Sources 71 (1998) 268.
[33] K. Yashiro, N. Yamada, T. Kawada, J. Hong, A. Kaimai, Y. Nigara, J. Mi Mizusaki, Demonstration and Stack Concept of Quick Startup/Shutdown SOFC (qSOFC) Electrochemistry, vol. 70, Tokyo, Japan, 2002, p. 958.
[34] T. Suzuki, T. Yamaguchi, Y. Fujishiro, M. Awano, J. Electrochem. Soc. 153 (5) (2006) A925–928.
[35] P.W. Li, M.K. Chyu, J. Power Sources 124 (2003) 487–498.
[36] Y. Lu, L. Schaefer, J. Power Sources 153 (2005) 68.
[37] P. Costamagna, Z. Selimovic, M.D. Borghi, et al., Chem. Eng. J. 102 (2004) 61–69.
[38] B. Borglum, Cell and stack development at Versa Power Systems, Presented at 10th Annual SECA Workshop, Pittsburgh, PA, July 14–16, 2009. Accessed 01-27-2010: http://www.netl.doe.gov/publications/proceedings/09/seca/presentations/Borglum_Presentation.pdf.
[39] H. Ghezel-Ayagh, B. Borglum, Coal-based SECA Program – FuelCell Energy Inc., Presented at 11th Annual SECA Workshop, Pittsburgh, PA, July 27–29, 2010. Accessed 10-8-2010: http://www.netl.doe.gov/publications/proceedings/10/seca/Abstracts/Borglum_Presentation.pdf.
[40] B.J. Koeppel, J.S. Vetrano, B.N. Nguyen, X. Sun, M.A. Khaleel, Ceram. Eng. Sci. Proc. 27 (2006) 325–335.
[41] W.N. Liu, X. Sun, M.A. Khaleel, Ceram. Eng. Sci. Proc. 29 (2009) 53–63.
[42] E. Achenbach, IEA Programme on RD&D on Advanced Fuel Cells – Annex II: Modeling and Evaluation of Advanced Solid Oxide Fuel Cells, Forschungszentrum Jülich, 31 March, 1996.
[43] E. Achenbach, J. Power Sources 49 (1994) 333–348.
[44] J-W. Kim, A.V. Virkar, K-Z. Fung, K. Mehta, S.C. Singhal, J. Electrochem. Soc. 146 (1) (1999) 69–78.
[45] L.A. Chick, J.W. Stevenson, K.D. Meinhardt, S.P. Simner, J.E. Jaffe, R.E. Williford, Modeling and performance of anode-supported SOFC, in: 2000 Fuel Cell Seminar-Abstracts, 2000, pp. 619–622.
[46] P.W. Li, M.K. Chyu, Electrochem. ASME J. Heat Transfer 127 (2005) 1344–1362.
[47] A. Weber, B. Sauer, A.C. Muller, D. Herbstritt, Ivers-Tiffee, Solid State Ionics 152–153 (2002) 543–550.
[48] Y. Matsuzaki, I. Yasuda, J. Electrochem. Soc. 147 (2000) 1630–1635.
[49] Lua, the programming language official site. Accessed 01-27-2010: http://www.lua.org.
[50] J. Larminie, A. Dicks, Fuel Cell Systems Explained, second ed., John Wiley & Sons Inc., West Sussex, England, 2003.
[51] J. Xu, G.F. Froment, AIChE J. 35 (1) (1989) 88–96.
[52] E. Achenbach, E. Riensche, J. Power Sources 52 (1994) 283–288.
[53] A.L. Dicks, K.D. Pointon, A. Siddle, J. Power Sources 86 (2000) 523–530.
[54] K. Ahmed, K. Foger, Catal. Today 63 (2000) 479–487.
[55] S. Singhal, K. Kendall, High Temperature Solid Oxide Fuel Cells: Fundamentals Design and Applications, Elsevier, 2003.
[56] S. Gordon, B.J. McBride, Computer Program for Calculation of Complex Chemical Equilibrium Compositions and Applications. 1. Analysis. NASA RP-1311, 1994.
[57] B.J. McBride, S. Gordon, Computer Program for Calculation of Complex Chemical Equilibrium Compositions and Applications: II. Users Manual and Program Description. NASA RP-131, 1996.
[58] R. Kerr, Delphi SOFC Stack Development Updated, Presented at 10th Annual SECA Workshop, Pittsburgh, PA, July 14–16, 2009. Accessed 01-27-2010: http://www.netl.doe.gov/publications/proceedings/09/seca/presentations/Kerr_Presentation.pdf.
[59] R.J. Braun, Optimal design and operation of solid oxide fuel cell systems for small-scale stationary applications, PhD thesis. University of Wisconsin-Madison (2002).
[60] J.R. Ferguson, J.M. Fiard, R. Herbin, J. Power Sources 58 (1996) 109–122.
[61] X. Zhang, J. Li, G. Li, Z. Feng, J. Power Sources 160 (2006) 258–267.
[62] A.C. Burt, I.B. Celik, R.S. Gemmen, A.V. Smirnov, J. Power Sources 126 (2004) 76–87.
[63] R.S. Gemmen, E. Liese, J. Rivera, F. Jabbari, J. Brouwer, Proceedings of the International Gas Turbine Institute Meeting of the American Society of Mechanical Engineers, May, 2000, pp. 8–12.
[64] A.C. Burt, I.B. Celik, R.S. Gemmen, A.V. Smirnov, Proceedings of the First International Conference on Fuel Cell Science, Engineering, and Technology, Rochester, New York, April, 2003, pp. 21–23.

[65] A.C. Burt, I.B. Celik, R.S. Gemmen, A.V. Smirnov, Proceedings of Eighth International Symposium on SOFC (SOFC-VIII), Paris, France, 27 April–2 May Rochester New York, April, 2003, pp. 21–23.
[66] F.P. Incropera, D.P. DeWitt, Introduction to Heat Transfer, John Wiley & Sons, 1990.
[67] H. Gheze-Ayagh and B. Borglum, Coal-Based SECA Program – Fuel-Cell Energy Inc., Presented at 11th Annual SECA Workshop, Pittsburgh, PA, July 27–29, 2010. Accessed 08-30-2010: http://www.netl.doe.gov/publications/proceedings/10/seca/Abstracts/Borglum_Presentation.pdf.